energy&fuels

pubs.acs.org/EF

Article

Influence of the Pore Structure on the Methane Adsorption Mechanism in the Upper Triassic Lacustrine Shales from the Western Sichuan Basin, China

Ziyi Liu, Dongxia Chen,* Siyuan Chang, Xiaoliang Wei, Xiuxiang Lv, Rusi Zuo, and Meiling Han

Cite This: *Energy Fuels* 2021, 35, 13654–13670

Read Online

ACCESS | Metrics & More | Article Recommendations

ABSTRACT: Diversity lithofacies in lacustrine shale possess different pore structures with different shale gas adsorption mechanisms. It is of great significance for lacustrine shale gas reserve prediction to clarify the adsorption mechanism of methane in lacustrine shales. A series of experiments was carried out on core samples from the Upper Triassic Xujiahe Formation in the western Sichuan Basin of China. CO_2 adsorption, N_2 adsorption, and scanning electron microscopy experiments were performed to analyze the pore structures of lacustrine shale. The pore structure of siliceous shale is more complex with higher values of pore fractal dimensions (D_1 and D_2) than other lithofacies, while, based on fitting curves to methane isothermal adsorption data, the method of the corrected Akaike's information criterion (AICc) measuring the goodness of the nonlinear fitting curves, pore structure, and analysis of methane adsorption layers are combined to evaluate and select methane adsorption model in this work. Additionally, the methane adsorption process could be described by a two combined first-order rate (TCFOR) model of adsorption rate. As shown by TCFOR in most samples, the normalized adsorption capacities of the fast process higher than that of the slow process ($Q_1 > Q_2$) appear during adsorption experiment. Thus, methane may not enter the micropores in large quantities under low experimental pressure (<10 MPa). The adsorption mechanism of methane in most samples is monolayer adsorption (Langmuir + Henry model) with the lower AICc value than other adsorption models. The DA + Henry model is suitable for the process of methane absorption in which the $Q_2 > Q_1$ appeared early in the methane adsorption experiment. Occasionally, the phenomenon of $Q_2 > Q_1$ could be found in the siliceous shale owing to the micropores dominating in it. Ultimately, the relationship between accumulated dV/dD (reflecting the density of different pore sizes) from N_2 adsorption experiment and the absolute adsorption amount (V_{abs}) calculated by models is figured out to determine the adsorption model of methane under different pore sizes. Methane adsorption in pores smaller than 3.4 nm is mainly a micropore filling mode, and filling of pores between 9.6 and 50 nm is mainly a monolayer mode. Nevertheless, the adsorption of methane in the pores between 3.4 and 9.6 nm is a transition from monolayer adsorption to micropore filling. The results enhance our understanding of the methane adsorption mechanisms in different lithofacies with different pore structures.

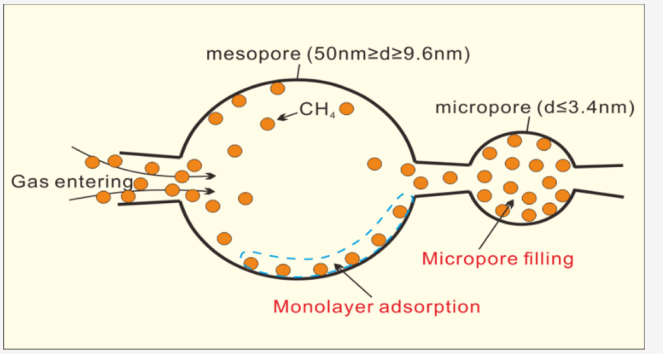

1. INTRODUCTION

The Upper Triassic Xujiahe Formation in the western Sichuan Basin, with proven gas reserves in place exceeding 3000×10^8 m^3 (including conventional and unconventional reservoirs), is considered to be the important lacustrine unconventional natural gas exploration target in Southwest China.[1−5] In order to increase production from lacustrine shales, the factors influencing the occurrences of adsorbed and free gas need to be clearly defined.[6,7] Shale gas is composed of free gas and adsorbed gas.[8−11] Among them, the adsorbed gas content could range from 20 to 85% of the total gas under reservoir conditions.[8] Thus, adsorbed gas could be a significant fraction of the total gas resource in shale gas reserves.

Traditionally, the adsorbed gas amount directly measured from isothermal adsorption experiments is known as the excess adsorption amount because the isothermal adsorption experiment could only test the adsorption amount exceeding the density of the gas phase.[12−14] However, the methane in most gas fields is in a supercritical state, where the density of the gas phase gradually approaches that of the adsorbed phase as the pressure increases. Consequently, the excess adsorption amount is not the true concentration of adsorbed methane.[14−17] As a result, several methane adsorption models based on Langmuir, Brunauer−Emmett−Teller (BET), Dubinin−Radushkevich (DR), and

Received: May 6, 2021
Revised: August 5, 2021
Published: August 20, 2021

Dubinin−Astakhov (DA) models have been used widely to gain insights into the methane adsorption mechanism to obtain the absolute adsorption amount of methane (i.e., the true adsorption amount of methane).[18−21] Among them, the DA model is an improved version of the DR model.[13,20] In order to figure out which model is suitable for methane adsorption in shale, the adsorption mechanism of methane should be clarified. By the grand canonical Monte Carlo (GCMC) method, the adsorption behavior of CH_4 in both organic and illite pores was simulated, and the molecular dynamics (MD) analysis was performed on the molecular structure at a certain temperature and pressure to document the adsorption mechanism.[22,23] The mineral composition, content of organic matter, thermal maturity of organic matter, adsorption temperature, and adsorption pressure were known as the parameters influencing the adsorption mechanism of methane in shales.[21,24−26] In addition, Rexer et al.[19] demonstrated that due to increased adsorption potentials in narrow pores, the DA-based model is more suitable for methane adsorption in micropores (pores with a diameter of < 2 nm), while the Langmuir-based model fits the methane adsorption data for mesopores (2−50 nm) in marine shale.

However, the MD analysis is more complicated and difficult to operate in the study of methane adsorption due to the complex model considered. In lacustrine shales, the lithofacies vary more frequently than in marine shales and the most suitable methane adsorption models need to incorporate this variability. To evaluate which model is the most suitable for methane adsorption in the western Sichuan Basin lacustrine shales, the evaluation method of the corrected Akaike's information criterion (AICc) was used for model selection instead of using the coefficient of determination (R^2).[14] For the AICc method, both goodness-of-fit and precision are used to measure the feasibility of statistical models. Meanwhile, the model with the lowest value of AICc is considered as the best suitable model.[27] Meanwhile, the AICc method is superior to using R^2 values from linear regression.[14,27,28] In addition, the adsorption model corresponding to different pore sizes in lacustrine shales will also differ from that in marine shales due to the differences between lacustrine and marine shales in other factors, particularly organic matter types and mineral compositions.

For determining the adsorption mechanism of methane in lacustrine shales, core samples are obtained from the Xujiahe Formation, the western Sichuan Basin, China. The data of X-ray diffraction (XRD) were used to identify the lithofacies in the lacustrine shale. Subsequently, N_2 adsorption and CO_2 adsorption experiments were carried out to determine the pore distributions in different lithofacies. The specific surface area (SSA) and the pore fractal dimensions (D_1 and D_2) were calculated from the adsorbed volume based on BET and Frenkel−Halsey−Hill (FHH) models, respectively,[29,30] and the pore development in different lithofacies was observed under the scanning electron microscope. Moreover, the methane isothermal adsorption experiments were carried out on samples of different lithofacies, and three types of methane adsorption models were used to interpret measured excess isotherms. Meanwhile, the AICc method was used for suitable methane adsorption model selection of different lithofacies. In order to explain why the model is suitable for the methane adsorption mechanism, the methane adsorption rate and layers were used to reveal the gas adsorption process and adsorbed behavior in the samples. Finally, the relationship between the absolute adsorption amount (V_{abs}) calculated by the suitable models and accumulated dV/dD (the change in pore volume as a function of change in pore diameter) from N_2 adsorption experiment was used to determine the most robust methane adsorption mode for a range of pore sizes.

2. GEOLOGICAL SETTING

The Sichuan Basin with an area of over 1.8×10^5 km^2 is one of the most prolific gas-productive basins located in southwestern China (Figure 1a).[31,32] In the western Sichuan Basin, shale gas is produced and well preserved mainly from the Mesozoic sediment (Figure 1a),[33] wherein the Upper Triassic Xujiahe Formation with a large resource potential is regarded as a key exploration target for lacustrine shale gas.[34,35] In the study area, the thickness of the Xujiahe Formation is about 700−1800 m, mainly composed of nearshore shallow lake and delta front deposits with shales, silty mudstone, argillaceous siltstone, fine/coarse grained sandstone, and coal seams (Figure 1b). The Xujiahe Formation consists of six members in an ascending order (i.e., T_3X^1, T_3X^2, T_3X^3, T_3X^4, T_3X^5, and T_3X^6 members) (Figure 1b), among which the T_3X^3 and T_3X^5 members are mainly dark gray to black continental shales, with coal seams (the coal seams are about 1.8−3.0 m) and a thin layer of gray fine-grained sandstones and siltstones.[36−38]

The bulk of the lacustrine-sourced natural gas in the Upper Triassic Xujiahe Formation is wet gas, with an average dryness coefficient of 0.93 (ranging from 0.83 to 0.98), which is similar to thermogenic gas generated from terrigenous, type III kerogen.[39] Potential gas source rocks include the T_3X^3 and T_3X^5 members.[33,40] The samples used in this study are from well LD1, which is located in the southwest of the Sichuan Basin (Figure 1a).

3. SAMPLES AND METHODS

Forty core samples were obtained from the T_3X^3 and T_3X^5 members in the well LD1, depth from 1160 to 1465 m. These sediments were mainly deposited in shallow lake environments. All samples were analyzed by XRD for mineralogy. Based on the mineral constituents, CO_2 and N_2 gas adsorption experiments were carried out on 25 samples, which is enough to present the pore structure of the different lithologies in the study area. Meanwhile, the methane isothermal adsorption curves were generated for the 25 samples, and the total organic carbon (TOC) was measured for the samples. In addition, the selected nine samples (three samples selected for each lithology as a representative) were studied under a scanning electron microscope for pore characteristics.

3.1. Total Organic Carbon. The TOC value of core samples was determined using a LECO CS-230 carbon analyzer at the China University of Petroleum (Beijing, China), and the experiment procedure adheres to the Chinese National Standard GB/T19145-2003. To remove the inorganic carbon, the core samples were crushed and sieved with an 80-mesh sieve and then reacted with 10 vol % HCl for 1 h. In this scenario, the measurement precision was estimated to be 0.45% of the measured TOC value.

3.2. X-ray Diffraction. The mineral contents were determined using a Bruker D8 Discover X-ray diffractometer.[41] The operational parameters and data processing techniques were those contained in the relevant oil-industry standard of China (SY/T 5163-2010). First, the core samples were crushed and centrifugally separated. Subsequently, the samples with a particle size smaller than 10 μm were used to evaluate the mineral content.

3.3. Scanning Electron Microscopy. To observe the characteristics of pores in lacustrine shale, SU8010 cold field emission scanning electron microscopy (SEM) equipped with low and high secondary-electron (SE) probes (1.0 nm/15 kV, 1.3 nm/1 kV) at China University of Petroleum (Beijing) was used to image the samples. It is worth noting that the core chips needed to be polished to 0.1 mm thickness using helium ion beams and cut into pieces measuring 0.5 cm × 1 cm × 0.2 mm before SEM imaging.

https://doi.org/10.1021/acs.energyfuels.1c01345
Energy Fuels 2021, 35, 13654−13670

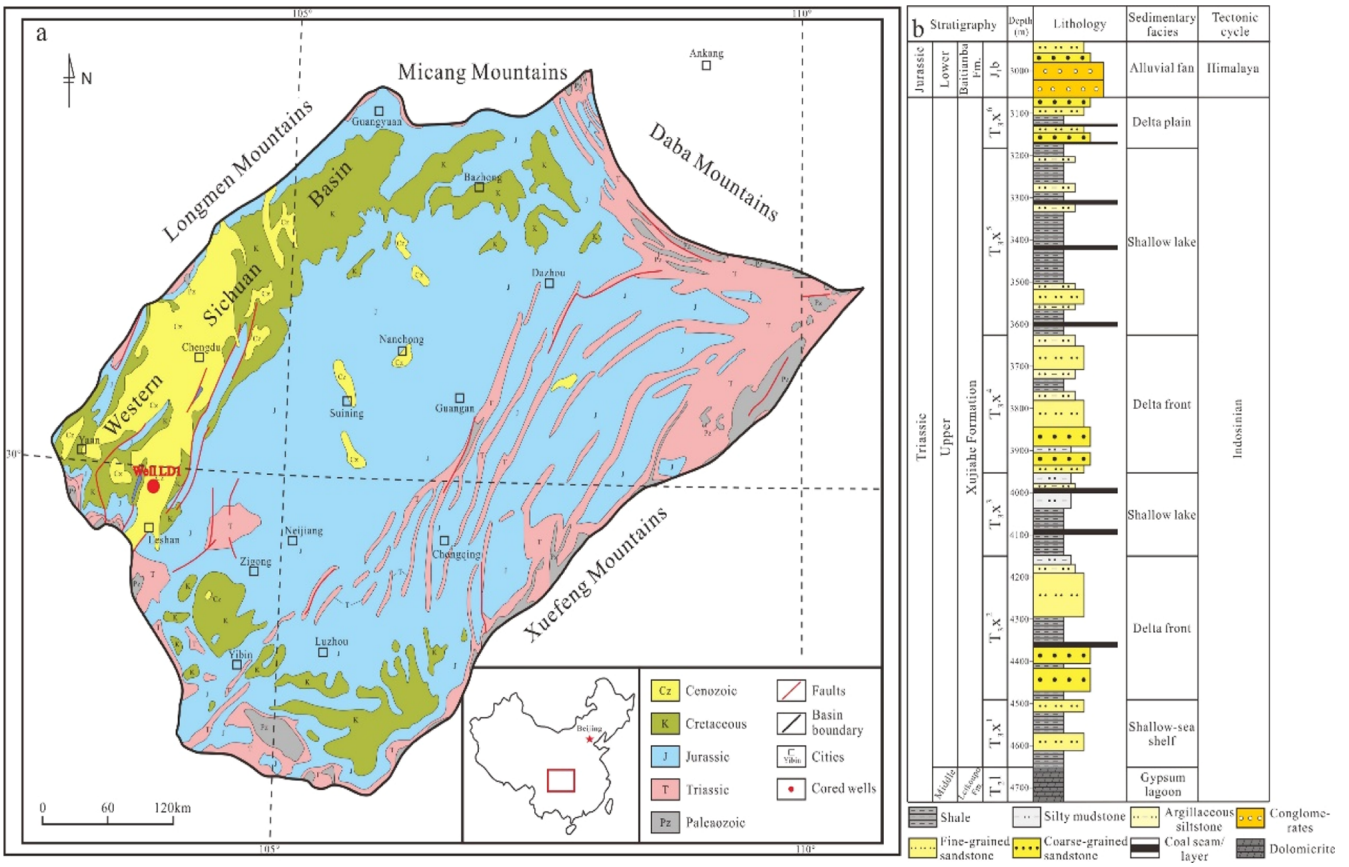

Figure 1. (a) Geological structure map of the Sichuan Basin (modified from Li et al.[3]) and (b) stratigraphic column of the Upper Triassic Xujiahe Formation in the western Sichuan Basin, southwest China (modified from Yang et al.[35]).

3.4. Low-Pressure CO_2 and N_2 gas Adsorption. The pore size distribution of lacustrine shale was measured by conducting nitrogen and carbon dioxide adsorption experiments with a Quantachrome Quadrasorb SI instrument at China University of Geoscience (Beijing, China). The adsorption isotherm measurements were performed at 77 K for N_2 and at 273 K for CO_2. The relative pressure ranged from 0.01 to 0.995 for N_2 and from 0.0001 to 0.032 for CO_2. CO_2 gas adsorption mainly reflects the characteristics of micropores (<2 nm). N_2 gas adsorption mainly reflects the characteristics of mesopores (between 2 and 50 nm). The analysis of CO_2 and N_2 adsorption with respect to pore size distribution must be run separately due to differences in calculation methods. For N_2 gas adsorption, the pore size distribution was obtained from the sorption curves in the pore size range of 2−50 nm using the Barrett−Joyner−Halenda method,[42,43] whereas the pore size distribution of micropores (<2 nm) obtained by CO_2 adsorption was interpreted using the density functional theory method.[44,45] Based on the BET method, the SSA was calculated from the sorption curve based on the adsorbed volume in a relative pressure (P/P_0) range of 0.05−0.35.[45,46] Additionally, fractal dimension values (D_1 and D_2) were calculated in the relative pressure (P/P_0) range of 0−0.5 and 0.5−1 using the FHH method.[47−49]

3.5. Methane Adsorption Experiments. The methane adsorption isotherms were obtained at 60 °C (average reservoir temperature of samples) using a 3H-2000PH isothermal adsorption apparatus, with 99.99% methane as a carrier gas. The apparatus (the adsorption system) consists of a sample cell and a reference cell connected through a two-way valve. Prior to the test, shale samples need to be pretreated and the process of the pretreatment was described in detail by Hu et al.[50] Then, the pretreated samples were placed into the sample cell, and the adsorption system was pressurized with helium gas to 14 MPa.[24,50] Subsequently, the adsorption system was evacuated, and the reference cell was introduced with methane. After the pressure variation less than 6.9×10^{-4} MPa over 5 min, the two-way valve was opened and the methane was expanded into the sample cell. By measuring the pressures before and after expansion in the reference cell, the molar density of the gas at different stages could be calculated using an appropriate equation of state. Meanwhile, the amount of gas adsorbed under a single pressure could be determined by the changes in pressures. Finally, the methane isotherm could be obtained by repeating these steps until the measured value at the highest required pressure is obtained.[18,24,50−52]

3.6. Multiple Models of Methane Adsorption. The Langmuir-based model could be used to describe the monolayer adsorption theory of methane on a solid surface.[14,24,53] According to previous research, both gas adsorption and absorption occur on polymers during gas adsorption.[54] Meanwhile, a hybrid model was proposed where the adsorption is modeled by the Langmuir component and the absorption is modeled by the Henry component.[54] Compared to the hybrid model, the adsorption models without the Henry component are prone to overestimating the adsorption phase density. It is unreasonable for the adsorption phase density is overestimated to be higher than the liquid density of methane (0.421 g/cm^3).[14] The model (Langmuir + Henry) is illustrated using the following equation[14,55]

$$V_{exc} = V_L \frac{\rho_{gas}}{\rho_L + \rho_{gas}}\left(1 - \frac{\rho_{gas}}{\rho_{ads}}\right) + k\rho_{gas}\left(1 - \frac{\rho_{gas}}{\rho_{ads}}\right) \quad (1)$$

where V_{exc} denotes the excess adsorption volume in m^3/t; the V_L is the Langmuir volume in cm^3/g; ρ_{gas} is the gas densities in the free gas in g/cm^3; ρ_L is the gas density at which the adsorption volume is half the Langmuir volume in g/cm^3; ρ_{ads} is the gas densities in the adsorbed phases in g/cm^3; and k is the coefficient of the absorption by the Henry component, dimensionless. Among them, ρ_{gas} could be obtained from the NIST (https://webbook.nist.gov/chemistry/fluid/) at the corresponding pressure and temperature.

https://doi.org/10.1021/acs.energyfuels.1c01345
Energy Fuels 2021, 35, 13654−13670

For molecular multilayer adsorption theory, the BET-based model is used in interpretation of excess adsorption isotherms.[14,46,55,56] The following is the BET-based model (BET + Henry) (eq 2)

$$V_{exc} = \frac{\rho_{gas}}{k_1 + k_2\rho_{gas} + k_3\rho_{gas}^2}\left(1 - \frac{\rho_{gas}}{\rho_{ads}}\right) + k\rho_{gas}\left(1 - \frac{\rho_{gas}}{\rho_{ads}}\right) \quad (2)$$

where $k_1 = P_0/V_L C$; $k_2 = (C - 2)/V_L C$; and $k_3 = (1 - C)/V_L C{\cdot}P_0$. Among them, P_0 is the saturation vapor pressure in MPa and C is the BET constant, dimensionless.

Additionally, the DA-based model is used in interpretation of the micropore filling theory.[14,46,55,56] The following is the DA-based model (DA + Henry) (eq 3)

$$V_{exc} = V_m \exp\left\{-D\left[\ln\left(\frac{\rho_{ads}}{\rho_{gas}}\right)\right]^n\right\}\left(1 - \frac{\rho_{gas}}{\rho_{ads}}\right) + k\rho_{gas}\left(1 - \frac{\rho_{gas}}{\rho_{ads}}\right) \quad (3)$$

where V_m is the maximum adsorption volume of micropore filling in cm^3/g; D is the adsorption characteristic parameter, dimensionless; and n is the coefficient related to the adsorption volume, dimensionless.

Based on the excess adsorption amount, the absolute adsorption amount could be calculated from[15]

$$V_{abs} = \frac{V_{exc}}{\left(1 - \frac{\rho_{gas}}{\rho_{ads}}\right)} \quad (4)$$

where V_{abs} is the absolute adsorption volume in m^3/t.

In the abovementioned models, the unknown parameters are ρ_{ads}, V_L, V_m, ρ_L, k, k_1, k_2, k_3, D, and n. All of them could be obtained by fitting the abovementioned models. The fitting parameters are obtained using the data analysis software Origin 2018 (OriginLab, USA). Additionally, the AICc could be used for model selection and is illustrated using the following equation[14]

$$AIC_C = N\ln\left(\frac{RSS}{N}\right) + 2K + \frac{2K(K+1)}{N - K - 1} \quad (5)$$

where N is the number of observations (i.e., the number of measured points for methane adsorption in this work); K is the number of fitted parameters; and RSS is the residual sum of squares and is defined as follows[14]

$$RSS = \sum (V_e - V_m)^2 \quad (6)$$

where V_e and V_m are the experimental and modeling results of excess adsorption amount, respectively.

3.7. Calculation of the Methane Adsorption Rate and Layer. During each pressure step of the methane adsorption experiments, the data of the methane adsorption rate could be estimated indirectly by monitoring the pressure drop at the same temperature.[14] The evaluation procedure of the adsorption rate was described in detail by Dang et al.,[14] and the methane adsorption rate could be calculated as

$$\frac{M_t}{M_\infty} = \frac{P_0 - P_t}{P_0 - P_\infty} \quad (7)$$

where M_t is the total adsorption of methane measured at time t in g; M_∞ is the total adsorption of methane measured at the infinite time in g (i.e., the adsorption no longer changes at this pressure); P_0 and P_∞ are the first and final pressure reading of a pressure step in MPa; and P_t is the gas pressure at time t. By plotting the fractional uptake M_t/M_∞ versus time t, the adsorption rate at each pressure step is obtained.

To interpret methane adsorption processes, a two combined first-order rate model (TCFOR model) will be used to interpret experimental adsorption rate data.[14,57] The expression of the TCFOR model is given as follows

$$Q_r(t) = [Q_1 \exp(-k't) + Q_2 \exp(-k''t)] \quad (8)$$

$$\frac{M_t}{M_\infty} = 1 - [Q_1\exp(-k't) + Q_2 \exp(-k''t)] \quad (9)$$

where $Q_r(t)$ is the normalized residual (unoccupied) adsorption capacity, dimensionless; Q_1 and Q_2 are the normalized adsorption capacities for the fast and slow process, respectively, as $Q_2 = 1 - Q_1$; and k' and k'' are the two first-order rate constants in s^{-1} for the fast and slow process, respectively.

In addition, methane adsorption in nanoscale pores has a certain number of adsorption layers. The number of methane molecular adsorption layers are calculated as follows[13]

$$\lambda = \frac{V_{abs} \times B_g}{10{,}000 \times S \times \sigma} \quad (10)$$

$$\sigma = \left(\frac{M_{CH_4}}{\rho_{ads} N_A}\right)^{1/3} \quad (11)$$

where λ is the number of adsorbed molecular layers, dimensionless; B_g is the formation gas compressibility coefficient, dimensionless; S is the SSA, m^2/g; σ is the average molecular size of adsorbed methane, cm; M_{CH_4} is the methane molar mass, g/mol; and N_A is the Avogadro constant, which is 6.022×10^{23} mol^{-1}.

4. RESULTS

4.1. Lithofacies Distribution of Xujiahe Formation Shales from Well LD1. The mineralogy and TOC contents of all samples analyzed are listed in Table 1. The TOC of the samples from the T_3X^3 member (varying from 0.49 to 2.16%, with an average value of 1.06%) is higher than that of the samples from the T_3X^5 member (varying from 0.26 to 1.30%, with an average value of 0.75%) (Figure 2). The XRD data reveal a range of mineral compositions of the samples, dominated by quartz and clay minerals (Figure 2 and Table 1). The quartz content ranges from 23.6 to 57.7% with an average of 38.6%, and the clay mineral content varies between 27.1 and 69.2% with an average of 48.2%. The feldspar and carbonate contents vary from 1.8 to 10% (average 5.4%) and 0 to 16.6% (average 7.8%), respectively. Based on the mineral constituents, the lithofacies distribution of lacustrine shales could be divided into three types (Figure 3), namely, siliceous shale (S, where the content of quartz and feldspar ≥50%), mixed shale (M, the content of quartz and feldspar <50%, the content of carbonate <50%, and clay mineral <50%), and argillaceous shale (AR, the content of clay mineral ≥50%).

4.2. Pore Structure of Xujiahe Formation Shales. Under SEM, interlayer pores within clays and organic matter pores (OM pores) mainly occur in argillaceous shale (Figure 4a,b). Meanwhile, there are hydrocarbon shrinkage cracks around and inside the OM (Figure 4c). For the siliceous shale, there are a small amount of intergranular pores and OM pores occurring in mineral particles and OM (Figure 4d–f). There are often some intercrystalline cracks around mineral particles (Figure 4d,f). In addition, the types of pores developed in the mixed shale are similar to those of the argillaceous shale, except the fact that there are fewer OM pores than argillaceous shale (Figure 4g–i).

In addition to different pore types, different lithologies have different pore structures. To describe the pore size distribution, the value of dV/dD is used to express the density of different pore sizes (Figure 5) and the data of cumulative dV/dD from N_2 adsorption experiment are used to express the cumulative density of different pore sizes in the samples (Figures 6 and 7). As shown in Figures 6 and 7, the cumulative dV/dD shows a significant increase (decrease) within a pore size of 10 nm and

https://doi.org/10.1021/acs.energyfuels.1c01345
Energy Fuels 2021, 35, 13654−13670

Table 1. Mineral Constituents, TOC, and Lithofacies of Samples in Well LD1[a]

			mineral composition content (%)					
sample	stratum	depth (m)	quartz	feldspar	carbonate	clay mineral	lithofacies	TOC (%)
LD1-1		1167.4	57.7	1.8	0.0	40.5	S	—
LD1-2	T_3x^5	1174.4	40.3	1.9	5.7	52.1	AR	0.55
LD1-3	T_3x^5	1183.4	33.2	2.9	11.4	52.5	AR	—
LD1-4	T_3x^5	1190.4	32.2	2.6	8.1	57.1	AR	0.66
LD1-5	T_3x^5	1199.4	27.5	2.9	13.8	55.8	AR	0.72
LD1-6	T_3x^5	1204.4	39.1	3.5	0.0	57.4	AR	0.48
LD1-7	T_3x^5	1215.4	23.6	2.6	4.6	69.2	AR	1.30
LD1-8	T_3x^5	1220.4	53.4	8.2	0.0	38.4	S	—
LD1-9	T_3x^5	1226.4	37.9	3.6	0.0	58.5	AR	0.19
LD1-10	T_3x^5	1237.4	38.8	4.3	8.8	48.1	M	—
LD1-11	T_3x^5	1239.4	47.7	7.8	6.0	38.5	S	0.90
LD1-12	T_3x^5	1243.4	49.4	7.0	7.3	36.3	S	0.26
LD1-13	T_3x^5	1245.4	36.7	3.1	16.6	43.6	M	—
LD1-14	T_3x^5	1249.4	32.1	3.2	9.8	54.9	AR	1.06
LD1-15	T_3x^5	1254.4	41.5	4.6	9.9	44.0	M	—
LD1-16	T_3x^5	1257.4	47.2	8.5	9.5	34.8	S	1.18
LD1-17	T_3x^5	1279.3	26.8	4.2	9.4	59.6	AR	—
LD1-18	T_3x^5	1294.3	36.6	6.1	14.5	42.8	M	0.90
LD1-19	T_3x^3	1341.5	44.5	6.0	4.8	44.7	S	—
LD1-20	T_3x^3	1344.5	41.2	10.0	3.6	45.2	S	0.92
LD1-21	T_3x^3	1348.5	56.5	5.9	10.5	27.1	S	—
LD1-22	T_3x^3	1350.5	41.3	5.5	8.7	44.5	M	1.01
LD1-23	T_3x^3	1353.0	39.0	5.5	0.0	55.5	AR	0.49
LD1-24	T_3x^3	1357.0	37.3	5.7	0.0	57.0	AR	0.80
LD1-25	T_3x^3	1359.0	33.9	6.6	0.0	59.5	AR	2.16
LD1-26	T_3x^3	1360.0	36.6	8.7	10.6	44.1	M	0.77
LD1-27	T_3x^3	1368.1	33.2	4.9	12.1	49.8	M	1.12
LD1-28	T_3x^3	1378.1	35.3	4.4	7.4	52.9	AR	0.90
LD1-29	T_3x^3	1383.1	46.0	8.0	12.5	33.5	S	—
LD1-30	T_3x^3	1392.1	29.1	6.6	13.1	51.2	AR	1.15
LD1-31	T_3x^3	1393.1	38.3	6.1	12.3	43.3	M	—
LD1-32	T_3x^3	1400.1	40.7	6.8	11.6	40.9	M	0.77
LD1-33	T_3x^3	1407.1	49.6	8.4	13.7	28.3	S	—
LD1-34	T_3x^3	1412.1	31.4	6.1	8.6	53.9	AR	1.12
LD1-35	T_3x^3	1418.1	37.4	6.0	10.3	46.3	M	—
LD1-36	T_3x^3	1429.7	31.9	4.7	10.0	53.4	AR	1.12
LD1-37	T_3x^3	1438.7	36.3	6.2	11.9	45.6	M	—
LD1-38	T_3x^3	1450.7	31.8	5.2	0.0	63.0	AR	1.40
LD1-39	T_3x^3	1456.7	29.0	5.3	6.3	59.4	AR	—
LD1-40	T_3x^3	1462.7	40.6	5.7	7.9	45.8	M	1.09

[a]— means not detected.

then flat out into a plateau region at a lager pore size. The pore size of samples is mostly within 10 nm. The pore size distribution of micropores is mainly characterized by CO_2 adsorption. For mesopores, the pore structure is characterized by N_2 adsorption. Here, three samples (LD1-28, LD1-11, and LD1-18) with a similar value of TOC were selected as representative samples of different lithofacies. As shown in Figure 5, micropores in the samples mainly range from 0.3 to 1.0 nm. Additionally, some mesopores occur in the samples mainly ranging from 3.0 to 6.0 nm. The data indicate that the argillaceous shale has more micropores and mesopores than other lithofacies (Figure 5). In terms of the pore fractal dimension, the values of D_1 and D_2 of mixed shale vary from 2.53 to 2.63 and 2.54 to 2.78, respectively. For the argillaceous shale, the values of D_1 and D_2 vary from 2.51 to 2.63 and 2.47 to 2.81, respectively. The pore structure of siliceous shale is more complex with values of D_1 and D_2 varying from 2.54 to 2.65 and 2.66 to 2.82, respectively (Figure 8). The values of D_1 and D_2 in the siliceous shale are higher than those of the argillaceous shale and mixed shale (Figures 8 and 9).

4.3. Isothermal Adsorption Curves and Modeling. The excess adsorption isotherms of methane from different lithofacies are determined by plotting the gas density against the excess adsorption volume (Figure 10). Based on the theory of Gibbs excess adsorption, the amount of adsorbed gas will increase first and then decrease under higher pressure.[12,19,25,58] However, increasing with the experiment pressure (the gas density), the amount of methane adsorbed in the samples increases under the low experiment pressure (<10 MPa) (Figure 10). In this work, the Langmuir + Henry, BET + Henry, and DA + Henry excess models were correlated with the excess isotherms to evaluate the suitable methane adsorption model for these lacustrine shales, and the modeling results of each model on shale samples are shown in Figure 10, and the fitting parameters of each model for samples from the well LD1 are shown in

https://doi.org/10.1021/acs.energyfuels.1c01345
Energy Fuels 2021, 35, 13654−13670

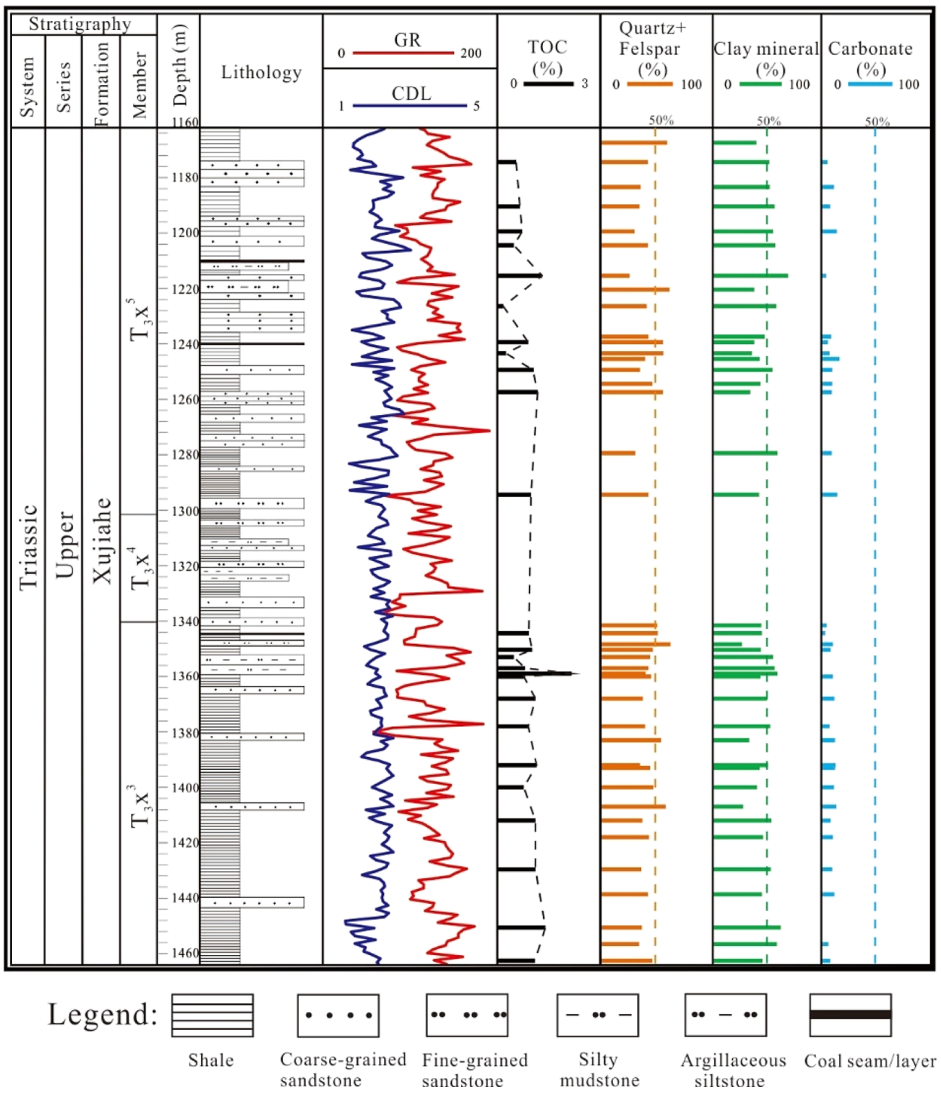

Figure 2. Lithology, mineral constituents, and TOC in well LD1.

Table 2. The adsorption contents from Langmuir + Henry excess models range from 0.21 to 1.32 cm^3/g and that from DA + Henry excess models range from 0.20 to 1.19 cm^3/g. The change in adsorption content from excess models is consistent with the change in TOC, which follows the characteristics of OM affecting adsorption capacity.

According to the isothermal adsorption, the AICc is used to determine the best fitting model for methane adsorption in the shale.[14,27] The values of AICc of three models are shown in Table 3. Except the sample LD1-12 and sample LD1-20, it could be found that the values of AICc in the siliceous shales are in the order Langmuir + Henry < DA + Henry < BET + Henry (Figure 11). However, the values of AICc are present in the order DA + Henry < Langmuir + Henry < BET + Henry in the sample LD1-12 and sample LD1-20 (Figure 11). For the argillaceous shales and mixed shales, it could be found that the values of AICc are in the order Langmuir + Henry < DA + Henry < BET + Henry (Figure 11). Under the low experiment pressure (<10 MPa), the different orders of model fitting could occur in the siliceous shales.

4.4. Methane Adsorption Process. In order to explain why the model is suitable for the methane adsorption mechanism, the methane adsorption rate was used to reveal

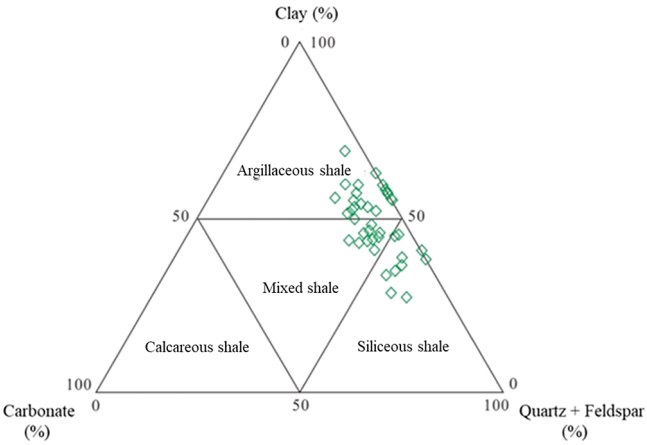

Figure 3. Classification scheme of shale lithofacies in Xujiahe Formations in well LD1.

the gas absorption processes in the shale, and the TCFOR model could be used to model the methane adsorption rate data. Six samples are selected as proxy for different lithofacies. It could be observed from the figure that the methane adsorption process is featured with two rate constants (Figure 12). To reach

https://doi.org/10.1021/acs.energyfuels.1c01345
Energy Fuels 2021, 35, 13654−13670

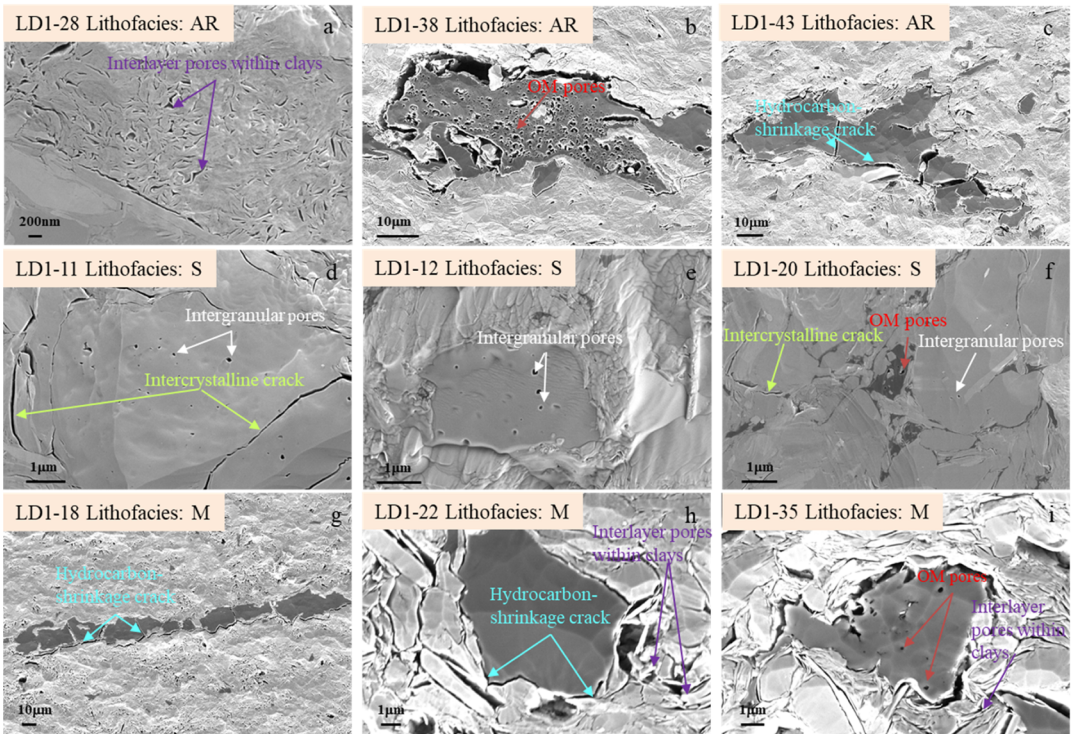

Figure 4. Pore development characteristics in different lithofacies of Xujiahe lacustrine shales. (a,h,i) Interlayer pores appear in clays of argillaceous shale and mixed shale, samples LD1-28, LD1-22, and LD1-35; (b,f,i) OM pores occur in argillaceous shale, siliceous shale, and mixed shale, samples LD1-38, LD1-20, and LD1-35; (c,g,h) hydrocarbon shrinkage cracks around and inside the OM, samples LD1-43, LD1-18, and LD1-22; (d−f) intergranular pores occur in mineral particles in siliceous shale, samples LD1-11, LD1-12, and LD1-20; and (d,f) intercrystalline cracks occur around mineral particles, samples LD1-11 and LD1-20.

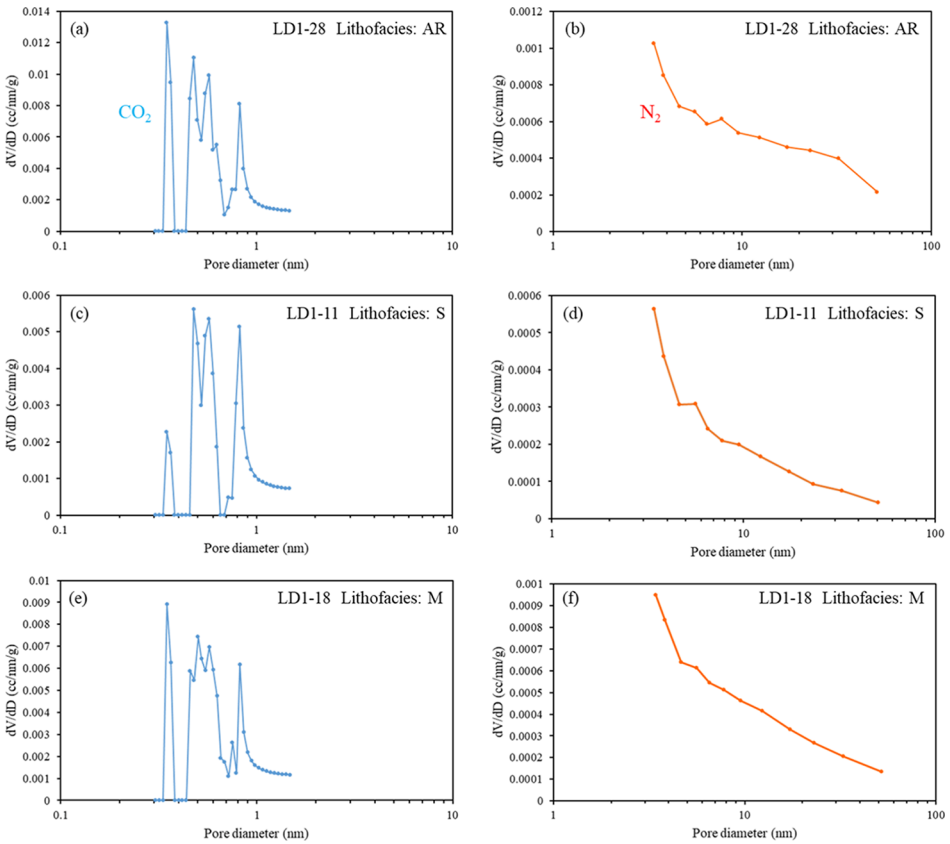

Figure 5. Pore size distribution of CO_2 and N_2 adsorption from different lithofacies in well LD1. (a,b) dV/dD vs pore diameter for argillaceous shale, sample LD1-28; (c,d) dV/dD vs pore diameter for siliceous shale, sample LD1-11; and (e,f) dV/dD vs pore diameter for mixed shale, sample LD1-18.

https://doi.org/10.1021/acs.energyfuels.1c01345
Energy Fuels 2021, 35, 13654−13670

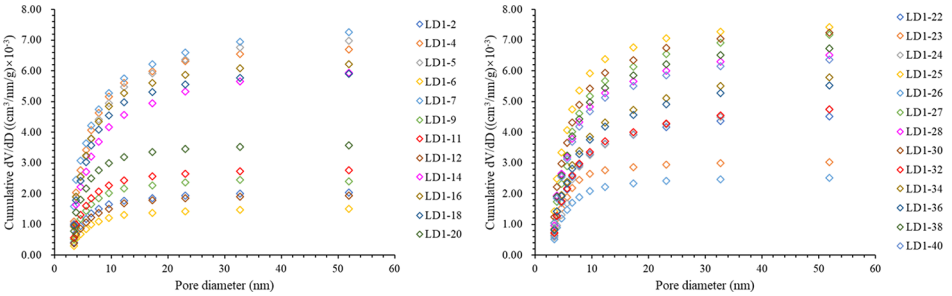

Figure 6. Data of cumulative dV/dD added up from small pores to large pores.

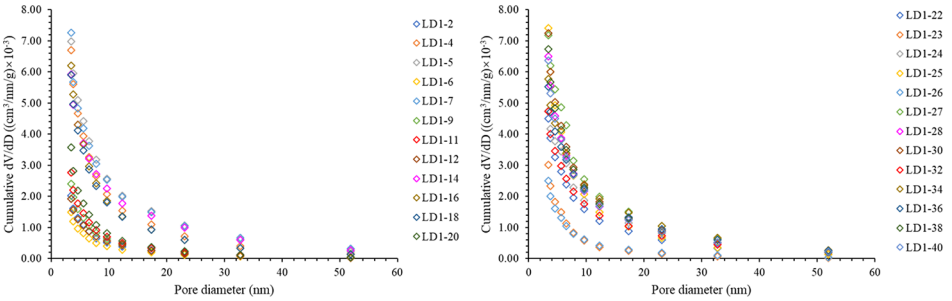

Figure 7. Data of cumulative dV/dD added up from large pores to small pores.

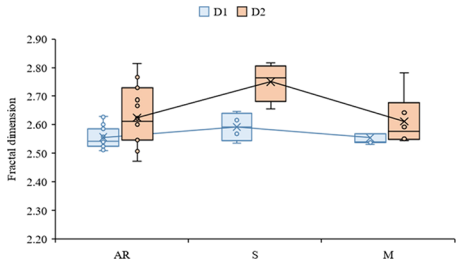

Figure 8. Fractal dimension of different lithofacies in well LD1.

adsorption equilibrium, the time increases with an increase in pressure steps. Meanwhile, the adsorption rate curves show a significant increase at early time (fast process) and then flat out into a plateau region (slow process) at higher pressure (Figure 12). This phenomenon may be attributed to the varied role of the different pore sizes in methane adsorption with increasing pressure steps.[44,59] Based on the data of the TCFOR model, the value of Q_1 decreases and Q_2 increases with the increase in the pressure (from 0.97 to 7.93 MPa) (Table 4). Here, the Q_1 and Q_2 represent the large pores and small pores dominating the adsorption process, respectively.[14] When the pressure is low, the gas molecules first enter the large pores in large quantities. As the pressure increases, the gas molecules enter the small pores. In terms of mesopores and micropores, methane will enter the mesopores first and then the micropores.

For sample LD1-12 and sample LD1-20 from the siliceous shale, the value of Q_1 decreases fast ranging from 0.83 to 0.35 and 0.81 to 0.37, respectively. The gas molecules are prone to entering the micropores during the methane isotherm adsorption process. However, the value of Q_1 of argillaceous shale decreases slowly, ranging from 0.86 to 0.71 and 0.91 to 0.75, respectively. For mixed shale, the rate of decrease of Q_1 is somewhere between the siliceous shale and argillaceous shale (ranging from 0.89 to 0.73 and 0.85 to 0.52, respectively) (Table 4).

4.5. Volume and Layer of Absolute Adsorption Gas.

Based on formation pressure, temperature, and ρ_{gas} (Table 5), the data for B_g were obtained by the NIST (https://webbook.nist.gov/chemistry/fluid/). Then, the V_{abs} calculated by the Langmuir + Henry model and DA + Henry model varies from 0.30 to 1.42 cm^3/g and 0.32 to 1.39 cm^3/g, respectively (Table 5). The V_{abs*} was the V_{abs} under formation conditions. According to eq 11, the adsorbed layers were calculated by the Langmuir + Henry model ranging from 0.94 to 1.85, which is similar to the result of calculation by the DA + Henry model ranging from 0.95 to 1.85 (Table 5). The number of adsorption layers calculated by

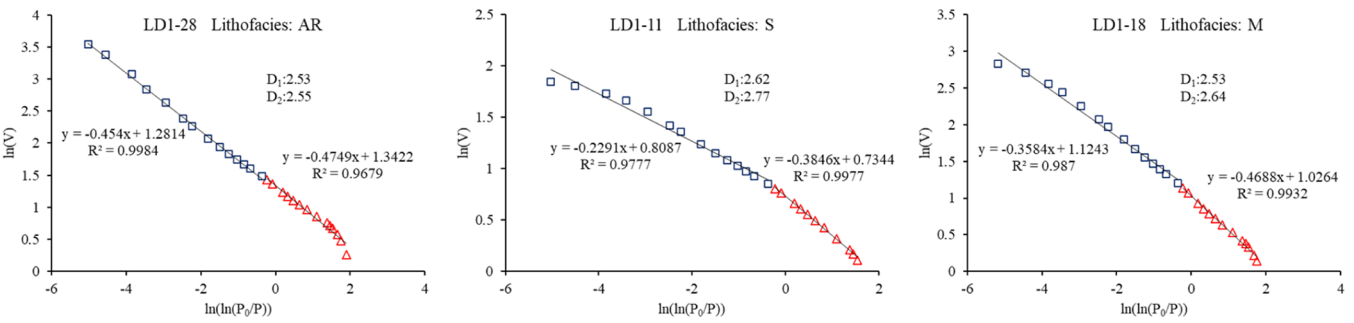

Figure 9. Calculated results of fractal dimensions with ln(V) vs ln(ln(P_0/P)) in different lithofacies.

https://doi.org/10.1021/acs.energyfuels.1c01345
Energy Fuels 2021, 35, 13654−13670

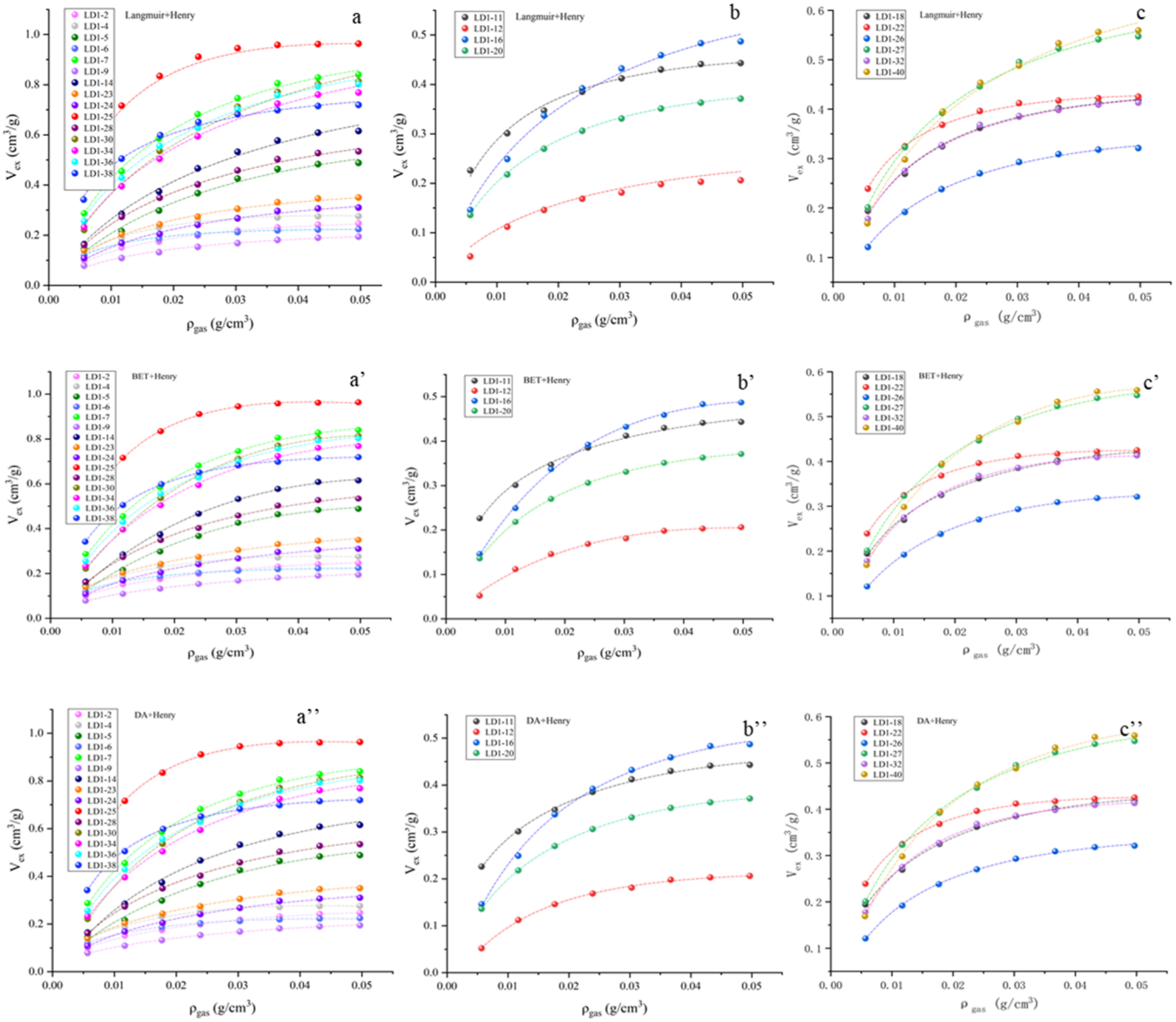

Figure 10. Characteristic of isothermal adsorption curves and modeling curves. (a,a′,a″) Langmuir + Henry, BET + Henry, and DA + Henry excess models of argillaceous shales; (b,b′,b″) Langmuir + Henry, BET + Henry, and DA + Henry excess models of siliceous shales; and (c,c′,c″) Langmuir + Henry, BET + Henry, and DA + Henry excess models of mixed shales.

Table 2. Fitting Parameters of Different Models in Methane Excess Adsorption on Shales from Well LD1[a]

models	sample	V_L/V_m (cm^3/g)	ρ_{ads} (g/cm^3)	ρ_L (g/cm^3)	k	k_1	k_2	k_3	D	n
Langmiur + Henry	LD1-2	0.27	0.19	0.013	2.34	——	——	——	——	——
	LD1-4	0.28	0.13	0.008	4.18	——	——	——	——	——
	LD1-5	0.56	0.21	0.025	5.78	——	——	——	——	——
	LD1-6	0.26	0.21	0.007	1.30	——	——	——	——	——
	LD1-7	0.98	0.25	0.016	6.62	——	——	——	——	——
	LD1-9	0.21	0.26	0.013	1.48	——	——	——	——	——
	LD1-11	0.49	0.24	0.008	2.78	——	——	——	——	——
	LD1-12	0.25	0.26	0.017	1.82	——	——	——	——	——
	LD1-14	0.64	0.26	0.021	6.84	——	——	——	——	——
	LD1-16	0.54	0.25	0.017	4.50	——	——	——	——	——
	LD1-18	0.49	0.27	0.010	2.13	——	——	——	——	——
	LD1-20	0.48	0.27	0.015	1.79	——	——	——	——	——
	LD1-22	0.48	0.26	0.006	2.00	——	——	——	——	——
	LD1-23	0.39	0.24	0.014	2.74	——	——	——	——	——
	LD1-24	0.34	0.25	0.016	2.73	——	——	——	——	——
	LD1-25	1.32	0.25	0.010	2.08	——	——	——	——	——

https://doi.org/10.1021/acs.energyfuels.1c01345
Energy Fuels 2021, 35, 13654−13670

Table 2. continued

models	sample	V_L/V_m (cm^3/g)	ρ_{ads} (g/cm^3)	ρ_L (g/cm^3)	k	k_1	k_2	k_3	D	n
	LD1-26	0.39	0.26	0.014	1.95	——	——	——	——	——
	LD1-27	0.59	0.27	0.012	4.25	——	——	——	——	——
	LD1-28	0.57	0.27	0.018	5.02	——	——	——	——	——
	LD1-30	0.86	0.27	0.019	8.17	——	——	——	——	——
	LD1-32	0.47	0.26	0.010	2.47	——	——	——	——	——
	LD1-34	0.79	0.27	0.016	7.57	——	——	——	——	——
	LD1-36	0.86	0.28	0.015	6.84	——	——	——	——	——
	LD1-38	0.76	0.28	0.007	4.50	——	——	——	——	——
	LD1-40	0.63	0.28	0.016	4.50	——	——	——	——	——
BET + Henry	LD1-2	——	0.14	——	5.09	0.03	6.96	−0.19	——	——
	LD1-4	——	0.11	——	6.83	0.02	5.16	−0.01	——	——
	LD1-5	——	0.16	——	0.11	0.04	0.57	−0.02	——	——
	LD1-6	——	0.17	——	2.30	0.03	4.44	−0.04	——	——
	LD1-7	——	0.21	——	4.33	0.02	0.77	−0.09	——	——
	LD1-9	——	0.22	——	2.77	0.05	7.54	−0.04	——	——
	LD1-11	——	0.22	——	4.48	0.01	2.52	−0.04	——	——
	LD1-12	——	0.17	——	1.19	0.09	1.64	−0.16	——	——
	LD1-14	——	0.23	——	5.08	0.03	1.12	−0.13	——	——
	LD1-16	——	0.21	——	0.32	0.03	0.93	−0.02	——	——
	LD1-18	——	0.24	——	3.14	0.02	2.28	−0.09	——	——
	LD1-20	——	0.22	——	2.40	0.03	2.12	−0.14	——	——
	LD1-22	——	0.23	——	2.04	0.01	2.01	−0.11	——	——
	LD1-23	——	0.21	——	4.99	0.03	4.01	−0.06	——	——
	LD1-24	——	0.21	——	4.01	0.05	3.74	−0.09	——	——
	LD1-25	——	0.23	——	0.03	0.01	0.67	−0.08	——	——
	LD1-26	——	0.24	——	1.11	0.04	2.10	−0.03	——	——
	LD1-27	——	0.25	——	2.96	0.02	1.40	−0.15	——	——
	LD1-28	——	0.24	——	3.81	0.03	1.37	−0.15	——	——
	LD1-30	——	0.19	——	0.00	0.02	0.45	−0.01	——	——
	LD1-32	——	0.21	——	1.83	0.02	1.77	−0.04	——	——
	LD1-34	——	0.24	——	0.51	0.02	0.62	−0.02	——	——
	LD1-36	——	0.26	——	2.88	0.02	0.79	−0.03	——	——
	LD1-38	——	0.24	——	2.51	0.01	1.07	−0.07	——	——
	LD1-40	——	0.24	——	0.23	0.03	0.89	−0.12	——	——
DA + Henry	LD1-2	0.25	0.17	——	2.94	——	——	——	0.15	1.60
	LD1-4	0.29	0.12	——	4.19	——	——	——	0.14	1.68
	LD1-5	0.52	0.17	——	6.49	——	——	——	0.21	1.68
	LD1-6	0.24	0.14	——	2.53	——	——	——	0.09	1.83
	LD1-7	0.91	0.21	——	6.93	——	——	——	0.07	2.24
	LD1-9	0.20	0.23	——	1.91	——	——	——	0.12	1.67
	LD1-11	0.45	0.23	——	3.41	——	——	——	0.04	2.18
	LD1-12	0.23	0.25	——	1.32	——	——	——	0.02	3.30
	LD1-14	0.62	0.24	——	5.78	——	——	——	0.07	2.39
	LD1-16	0.51	0.23	——	3.73	——	——	——	0.04	2.64
	LD1-18	0.46	0.23	——	2.69	——	——	——	0.05	2.22
	LD1-20	0.42	0.21	——	2.58	——	——	——	0.07	2.22
	LD1-22	0.45	0.24	——	2.16	——	——	——	0.01	3.02
	LD1-23	0.37	0.23	——	3.25	——	——	——	0.11	1.75
	LD1-24	0.32	0.24	——	2.86	——	——	——	0.09	2.00
	LD1-25	1.19	0.23	——	2.41	——	——	——	0.02	2.88
	LD1-26	0.33	0.24	——	2.26	——	——	——	0.03	2.72
	LD1-27	0.56	0.24	——	4.16	——	——	——	0.04	2.50
	LD1-28	0.54	0.25	——	4.76	——	——	——	0.07	2.27
	LD1-30	0.83	0.23	——	6.88	——	——	——	0.05	2.62
	LD1-32	0.43	0.24	——	2.43	——	——	——	0.02	3.01
	LD1-34	0.78	0.23	——	6.88	——	——	——	0.06	2.38
	LD1-36	0.83	0.24	——	6.38	——	——	——	0.05	2.44
	LD1-38	0.73	0.25	——	4.16	——	——	——	0.01	3.24
	LD1-40	0.59	0.26	——	3.71	——	——	——	0.03	2.77

[a] V_L/V_m means V_L used in Langmiur + Henry and V_m used in DA + Henry. — means not applicable.

https://doi.org/10.1021/acs.energyfuels.1c01345
Energy Fuels 2021, 35, 13654−13670

Table 3. Evaluation of Different Methane Adsorption Models by the ACI_C Method

models	sample	AIC_C	RSS	*N*	*K*	sample	AIC_C	RSS	*N*	*K*
Langmiur + Henry	LD1-2	−66.10430	0.00014	8	4	LD1-23	−58.71129	0.00036	8	4
	LD1-4	−65.02715	0.00016	8	4	LD1-24	−64.29454	0.00018	8	4
	LD1-5	−49.42679	0.00115	8	4	LD1-25	−47.71195	0.00143	8	4
	LD1-6	−74.52491	0.00005	8	4	LD1-26	−69.23853	0.00010	8	4
	LD1-7	−52.02872	0.00083	8	4	LD1-27	−58.62336	0.00037	8	4
	LD1-9	−68.80785	0.00010	8	4	LD1-28	−57.92214	0.00040	8	4
	LD1-11	−58.65567	0.00036	8	4	LD1-30	−42.63797	0.00269	8	4
	LD1-12	−56.04681	0.00050	8	4	LD1-32	−59.30008	0.00034	8	4
	LD1-14	−48.49271	0.00130	8	4	LD1-34	−47.40839	0.00148	8	4
	LD1-16	−53.70967	0.00067	8	4	LD1-36	−51.58204	0.00088	8	4
	LD1-18	−66.10343	0.00014	8	4	LD1-38	−51.02975	0.00094	8	4
	LD1-20	−76.13590	0.00004	8	4	LD1-40	−51.11872	0.00093	8	4
	LD1-22	−75.45683	0.00004	8	4					
BET + Henry	LD1-2	−51.08774	0.00009	8	5	LD1-23	−43.97726	0.00022	8	5
	LD1-4	−34.31155	0.00074	8	5	LD1-24	−40.40673	0.00035	8	5
	LD1-5	−28.02422	0.00162	8	5	LD1-25	−1.496021	0.04471	8	5
	LD1-6	−43.21510	0.00024	8	5	LD1-26	−38.37384	0.00045	8	5
	LD1-7	−14.09032	0.00926	8	5	LD1-27	−25.50900	0.00222	8	5
	LD1-9	−57.53121	0.00004	8	5	LD1-28	−28.12781	0.00160	8	5
	LD1-11	−24.08542	0.00266	8	5	LD1-30	−10.67505	0.01419	8	5
	LD1-12	−26.12878	0.00206	8	5	LD1-32	−28.42333	0.00154	8	5
	LD1-14	−18.62147	0.00526	8	5	LD1-34	−19.98391	0.00443	8	5
	LD1-16	−22.26096	0.00334	8	5	LD1-36	−25.15086	0.00232	8	5
	LD1-18	−46.27229	0.00017	8	5	LD1-38	−31.41482	0.00106	8	5
	LD1-20	−35.95796	0.00060	8	5	LD1-40	−19.86138	0.00450	8	5
	LD1-22	−22.26588	0.00333	8	5					
DA + Henry	LD1-2	−55.94052	0.00005	8	5	LD1-23	−49.87669	0.00011	8	5
	LD1-4	−48.07023	0.00013	8	5	LD1-24	−46.27170	0.00017	8	5
	LD1-5	−32.10751	0.00097	8	5	LD1-25	−28.38208	0.00155	8	5
	LD1-6	−54.63656	0.00006	8	5	LD1-26	−56.27488	0.00005	8	5
	LD1-7	−29.17766	0.00140	8	5	LD1-27	−40.10087	0.00036	8	5
	LD1-9	−60.99290	0.00003	8	5	LD1-28	−36.00548	0.00060	8	5
	LD1-11	−35.53625	0.00063	8	5	LD1-30	−35.67662	0.00062	8	5
	LD1-12	−62.55333	0.00002	8	5	LD1-32	−32.58480	0.00092	8	5
	LD1-14	−31.70672	0.00102	8	5	LD1-34	−31.18589	0.00109	8	5
	LD1-16	−27.59022	0.00171	8	5	LD1-36	−31.15017	0.00110	8	5
	LD1-18	−49.67833	0.00011	8	5	LD1-38	−33.05251	0.00087	8	5
	LD1-20	−79.58893	0.000003	8	5	LD1-40	−27.09292	0.00182	8	5
	LD1-22	−27.44235	0.00175	8	5					

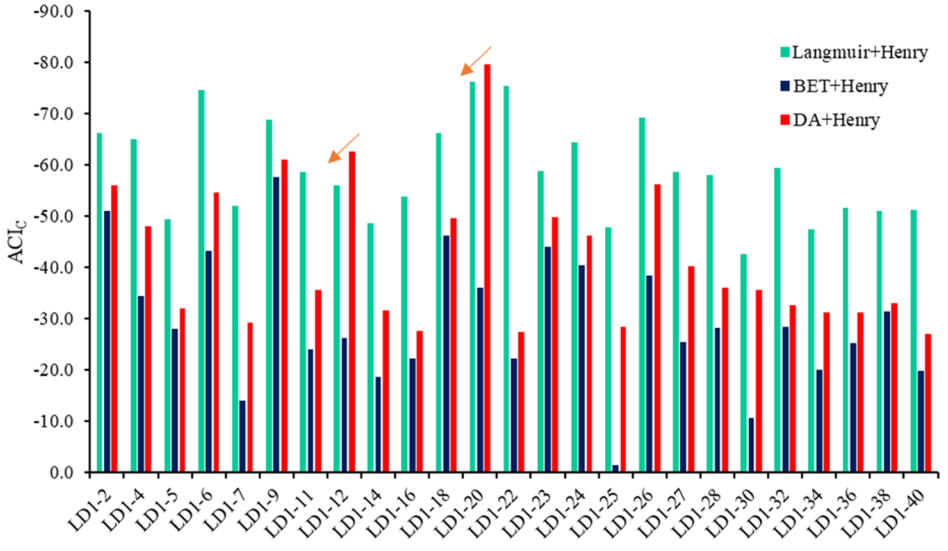

Figure 11. ACI_C of different methane adsorption models. Only in the sample LD1-12 and sample LD1-20, the values of AICc are present in the order DA + Henry < Langmuir + Henry < BET + Henry.

https://doi.org/10.1021/acs.energyfuels.1c01345
Energy Fuels 2021, 35, 13654−13670

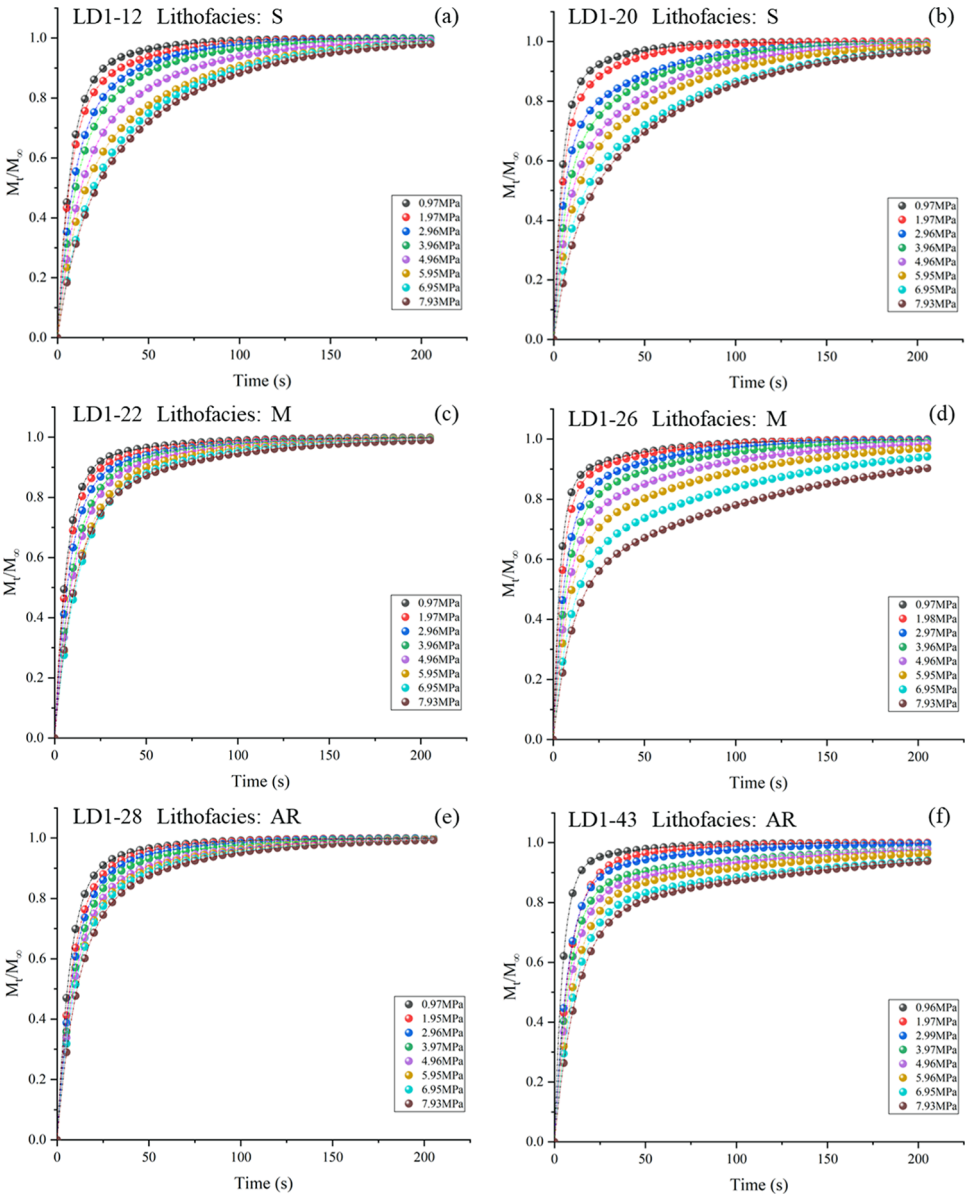

Figure 12. Adsorption rate curves of eight pressure steps for the samples from the well LD1. (a,b) M_t/M_∞ vs time for siliceous shale, sample LD1-12 and sample LD1-20; (c,d) M_t/M_∞ vs time for mixed shale, sample LD1-22 and sample LD1-26; and (e,f) M_t/M_∞ vs time for argillaceous shale, sample LD1-28 and sample LD1-43.

the two models is between one and two layers (Figure 13). Additionally, whether the V_{abs} is calculated by the Langmuir + Henry model or DA + Henry model, the plot of V_{abs} to SSA shows a relatively positive correlation (Figure 14). Hence, the pore structure, especially the SSA, will affect the volumes of absolute adsorption.

5. DISCUSSION

5.1. Suitable Methane Adsorption Model for Lacustrine Shales in Well LD1. Based on the data of the AICc (Table 3), the DA + Henry models for sample LD1-12 and sample LD1-20 have the lowest AICc values. Hence, the DA + Henry models are appropriate for modeling the mechanism of methane absorption in these two samples. For other samples, the mechanism of methane adsorption follows Langmuir + Henry models with the lowest AICc values. According to the methane adsorption rate curves (Figure 12), the phenomenon of $Q_2 > Q_1$ appeared earlier under the lower pressure (5.95 MPa) in the samples (e.g., sample LD1-12 and sample LD1-20) which are suitable for the DA + Henry model, and the methane molecules are prone to entering in micropores, whereas the phenomenon of $Q_1 > Q_2$ appears in other samples during the whole methane adsorption which are suitable for Langmuir + Henry models (Table 4).

Because the experimental adsorption pressure only reached 7.93 MPa, which is lower than formation pressure, methane may not enter the micropores in large quantities, resulting in the phenomenon of $Q_1 > Q_2$ appearing for the whole of the methane adsorption. However, gas adsorption mainly occurs in micropores because of a high surface area, especially at low pressure. With a small amount of methane entering the micropores, there may only be enough a layer of methane molecules in the micropores. Thus, the samples with the phenomenon of $Q_1 > Q_2$ are suitable for Langmuir + Henry models. As the pressure increases, more methane will enter the micropore which may show a mode of micropore filling. For sample LD1-12 and

https://doi.org/10.1021/acs.energyfuels.1c01345
Energy Fuels 2021, 35, 13654−13670

Table 4. Fitting Parameters of the TCFOR Model for the Methane Adsorption Process

sample	Q_1	Q_2	k' (s^{-1})	k'' (s^{-1})	sample	Q_1	Q_2	k' (s^{-1})	k'' (s^{-1})
LD1-12	0.83	0.17	0.143	0.0306	LD1-26	0.85	0.15	0.263	0.0246
	0.74	0.26	0.152	0.0287		0.83	0.17	0.211	0.0238
	0.67	0.33	0.123	0.0273		0.78	0.22	0.165	0.0211
	0.63	0.37	0.111	0.0241		0.74	0.26	0.149	0.0181
	0.56	0.44	0.098	0.0198		0.69	0.31	0.136	0.0147
	0.47	0.53	0.102	0.0174		0.64	0.36	0.124	0.0121
	0.41	0.59	0.082	0.0176		0.58	0.42	0.105	0.0096
	0.35	0.65	0.091	0.0172		0.52	0.48	0.098	0.0078
LD1-20	0.81	0.19	0.228	0.0375	LD1-28	0.86	0.14	0.147	0.0283
	0.73	0.27	0.217	0.0346		0.84	0.16	0.124	0.0267
	0.66	0.34	0.194	0.0221		0.83	0.17	0.116	0.0238
	0.58	0.42	0.165	0.0227		0.81	0.19	0.107	0.0214
	0.52	0.48	0.148	0.0198		0.77	0.23	0.105	0.0191
	0.48	0.52	0.131	0.0176		0.76	0.24	0.098	0.0182
	0.42	0.58	0.119	0.0146		0.74	0.26	0.101	0.0178
	0.37	0.63	0.096	0.0148		0.71	0.29	0.092	0.0181
LD1-22	0.89	0.11	0.154	0.0232	LD1-43	0.91	0.09	0.218	0.0292
	0.86	0.14	0.146	0.0217		0.88	0.12	0.127	0.0251
	0.84	0.16	0.126	0.0204		0.86	0.14	0.139	0.0184
	0.82	0.18	0.104	0.0205		0.85	0.15	0.124	0.0096
	0.81	0.19	0.098	0.0186		0.82	0.18	0.114	0.0101
	0.79	0.21	0.083	0.0175		0.81	0.19	0.096	0.0082
	0.75	0.25	0.082	0.0168		0.78	0.22	0.091	0.0064
	0.73	0.27	0.092	0.0161		0.75	0.25	0.082	0.0068

Table 5. Volume and Layer of Absolute Adsorption Gas[a]

								V_{abs} (cm^3/g)		V_{abs*} (cm^3/g)		adsorbed layers	
samples	depth (m)	formation pressure (MPa)	formation temperature (°C)	B_g	SSA (m^2/g)	ρ_{gas} (g/cm^3)	σ (cm)	L + H	DA + H	L + H	DA + H	L + H	DA + H
LD1-2	1174.4	11.51	55.23	0.00876	6.96	0.0755	5.19×10^{-8}	0.41	0.45	0.0036	0.0039	0.99	1.05
LD1-4	1190.4	11.67	55.71	0.00866	7.89	0.0765	5.89×10^{-8}	0.57	0.60	0.0049	0.0052	1.06	1.09
LD1-5	1199.4	11.75	55.98	0.00860	11.64	0.0769	5.02×10^{-8}	0.87	0.95	0.0075	0.0082	1.28	1.30
LD1-6	1204.4	11.80	56.13	0.00857	3.99	0.0772	5.02×10^{-8}	0.34	0.43	0.0029	0.0037	1.45	1.61
LD1-7	1215.4	11.91	56.46	0.00850	13.79	0.0778	4.74×10^{-8}	1.33	1.39	0.0113	0.0118	1.73	1.71
LD1-9	1226.4	12.02	56.79	0.00843	5.12	0.0785	4.68×10^{-8}	0.30	0.32	0.0025	0.0027	1.06	1.08
LD1-11	1239.4	12.15	57.18	0.00836	8.16	0.0792	4.80×10^{-8}	0.67	0.70	0.0056	0.0058	1.43	1.47
LD1-12	1243.4	12.19	57.30	0.00833	4.35	0.0795	4.68×10^{-8}	0.35	0.33	0.0029	0.0027	1.43	1.33
LD1-14	1249.4	12.24	57.48	0.00830	10.86	0.0797	4.68×10^{-8}	1.05	1.03	0.0087	0.0085	1.72	1.64
LD1-16	1257.4	12.32	57.72	0.00825	8.72	0.0802	4.74×10^{-8}	0.81	0.79	0.0067	0.0065	1.62	1.54
LD1-18	1294.3	12.68	58.83	0.00805	9.81	0.0822	4.62×10^{-8}	0.61	0.66	0.0049	0.0053	1.08	1.11
LD1-20	1344.5	13.18	60.34	0.00779	10.1	0.085	4.62×10^{-8}	0.56	0.62	0.0044	0.0048	0.94	0.95
LD1-22	1350.5	13.23	60.52	0.00776	6.27	0.0853	4.68×10^{-8}	0.62	0.63	0.0048	0.0049	1.64	1.62
LD1-23	1353.0	13.26	60.59	0.00775	6.24	0.0855	4.80×10^{-8}	0.57	0.61	0.0044	0.0047	1.47	1.56
LD1-24	1357.0	13.30	60.71	0.00773	6.82	0.0857	4.74×10^{-8}	0.52	0.54	0.0040	0.0042	1.24	1.28
LD1-25	1359.0	13.32	60.77	0.00772	12.13	0.0858	4.74×10^{-8}	1.36	1.37	0.0105	0.0106	1.83	1.79
LD1-26	1360.0	13.33	60.80	0.00772	5.91	0.0858	4.68×10^{-8}	0.50	0.51	0.0039	0.0039	1.40	1.39
LD1-27	1368.1	13.41	61.04	0.00768	12.17	0.0863	4.62×10^{-8}	0.88	0.90	0.0068	0.0069	1.20	1.18
LD1-28	1378.1	13.51	61.34	0.00763	10.6	0.0868	4.62×10^{-8}	0.91	0.91	0.0069	0.0069	1.42	1.38
LD1-30	1392.1	13.64	61.76	0.00757	13.81	0.0875	4.62×10^{-8}	1.42	1.39	0.0107	0.0105	1.69	1.56
LD1-32	1400.1	13.72	62.00	0.00753	7.65	0.0879	4.68×10^{-8}	0.64	0.63	0.0048	0.0047	1.35	1.29
LD1-34	1412.1	13.84	62.36	0.00748	12.12	0.0886	4.62×10^{-8}	1.34	1.35	0.0100	0.0101	1.79	1.71
LD1-36	1429.7	14.01	62.89	0.00741	11.87	0.0895	4.56×10^{-8}	1.35	1.36	0.0100	0.0101	1.85	1.77
LD1-38	1450.7	14.22	63.52	0.00732	11.41	0.0906	4.56×10^{-8}	1.11	1.10	0.0081	0.0080	1.56	1.49
LD1-40	1462.7	14.33	63.88	0.00727	10.72	0.0912	4.56×10^{-8}	0.95	0.91	0.0069	0.0066	1.41	1.32

[a] V_{abs*} is the V_{abs} under formation conditions, $V_{abs*} = V_{abs} \times B_g$. L + H is the Langmiur + Henry model, and DA + H is the DA + Henry model.

sample LD1-20, both of them are siliceous shales, the pores in it are not well developed as in argillaceous shale and mixed shale (Figures 4 and 5). However, the proportion of micropores in siliceous shales is higher than that of micropores in argillaceous shale and mixed shale, showing a high value of fractal dimension. Due to the micropore structure complexed with a high value of

https://doi.org/10.1021/acs.energyfuels.1c01345
Energy Fuels 2021, 35, 13654−13670

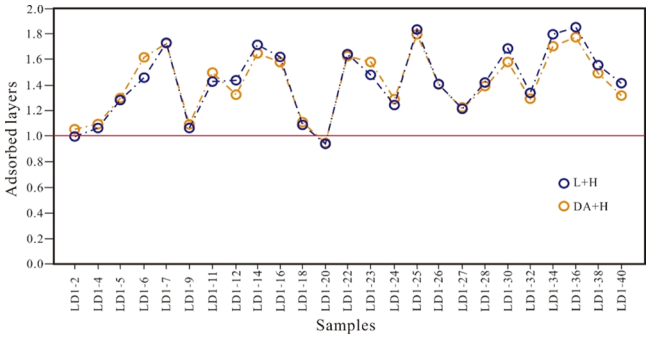

Figure 13. Methane adsorption layer in the samples from the well LD1.

fractal dimension (Figure 8), micropores have greater influence on the pore structure in siliceous shale than other lithofacies. Hence, during methane adsorption, the methane molecules in siliceous shales may enter the micropores earlier in a large amount. Furthermore, it may be shown as the mode of micropore filling under the lower pressure (e.g., the phenomenon of methane adsorption in sample LD1-12 and sample LD1-20).

Additionally, not all methane adsorption in siliceous shale fits the DA + Henry model under low pressure. This may be because the methane adsorption rate is not only affected by the pore structure, whereas the methane adsorption mode is affected by the pore structure. For example, the micropore filling mode is suitable for gas filling in the micropores. The adsorption mode of methane in the mesopores is mainly followed by monolayer adsorption.

5.2. Adsorption Mechanism of Methane under Different Pore Sizes. Methane is commonly adsorbed in shale pores in two different processes: micropore filling or monolayer adsorption.[12,14] Accordingly, the methane molecules adsorbed in the samples from the well LD1 also show the characteristics of micropore filling or monolayer adsorption, and the number of adsorption layers is less than 2 but not strictly 1 (Figure 13). Due to the existence of the micropore filling, the number of adsorption layers is not strictly 1. Previous studies of supercritical gas sorption in marine shales have shown that gas is adsorbed in micropores (pores with a diameter of < 2 nm) due to increased adsorption potentials in narrow pores.[19] In mesopores (2−50 nm), methane is mainly adsorbed in the pores in the form of monolayer adsorption.[19,60] However, in lacustrine shales, the pore size range corresponding to the methane adsorption mode will be different from that of the marine shales. Because of the SSA affecting the volume of absolute adsorption gas (Figure 14), the density of different pore sizes will affect the amount of adsorbed gas.

In this work, the data of cumulative dV/dD from the N_2 adsorption experiment are used to express the cumulative density of different pore sizes in the samples (Figures 6 and 7). Then, the data of cumulative dV/dD and the V_{abs} (calculated by Langmuir + Henry or DA + Henry models) were linear regression fitted to determine the adsorption mode for methane in a range of pore sizes. During the process of the linear regression fitting, the cumulative dV/dD values started to add up from small pores to large pores for the DA + Henry model (Figure 6), while for the Langmuir + Henry model, the cumulative dV/dD values added up from large pores to small pores (Figure 7). Based on the result of the linear regression fitting, the pore diameter with the highest value of R^2 determined by the micropore filling mode (DA + Henry model) is 3.4 nm (Figure 15a). For the monolayer adsorption mode (Langmuir + Henry model), the pore diameter with the highest value of R^2 is determined to be 9.6 nm (Figure 15b). Therefore, the micropore filling mode is mainly suitable for the methane adsorption in pores smaller than 3.4 nm, and the monolayer adsorption model is more in line with pores between 9.6 and 50.0 nm (Figure 16). In addition, the intermediate region between 3.4 and 9.6 nm is the transition zone where the monolayer adsorption changes to micropore filling as the pore diameter decreases (Figure 16).

6. CONCLUSIONS

The Xujiahe lacustrine shales are composed of three types of lithofacies: siliceous shales, argillaceous shales, and mixed shales. The proportion of micropores in siliceous shales is higher than that of micropores in argillaceous shale and mixed shale. Under low experimental pressure (<10 MPa), the processes of methane adsorption in some siliceous shale are prone to the corresponding DA + Henry model, Whereas not all methane adsorption in siliceous shale fits the DA + Henry model under low experimental pressure. Based on the analysis of the methane adsorption rate, the phenomenon of $Q_2 > Q_1$ appeared early in these siliceous shales and the phenomenon of $Q_1 > Q_2$ appeared in other samples which are suitable for the Langmuir + Henry model. Moreover, the methane molecules adsorbed in the samples from the well LD1 also show the characteristics of micropore filling or monolayer adsorption, and the number of adsorption layers is between one and two layers.

The overall adsorption of methane in shale shows monolayer adsorption (Langmuir + Henry model) or micropore filling (DA + Henry model). Besides, the methane adsorption mode in different pores is also different. For marine shales, the DA + Henry models are suitable for gas filling in the micropores. The mechanism of gas adsorption in the mesopores mainly follows Langmuir + Henry models. However, it is different from marine shales that micropore filling also occurs in some of the mesopores in lacustrine shales in

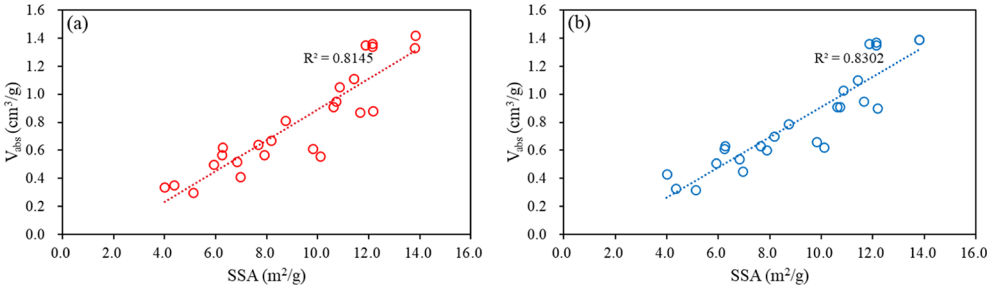

Figure 14. Factors influencing the absolute volumes of adsorbed gas: (a) relationship between SSA and V_{abs} calculated by the Langmuir + Henry model and (b) relationship between SSA and V_{abs} calculated by the DA + Henry model.

https://doi.org/10.1021/acs.energyfuels.1c01345
Energy Fuels 2021, 35, 13654−13670

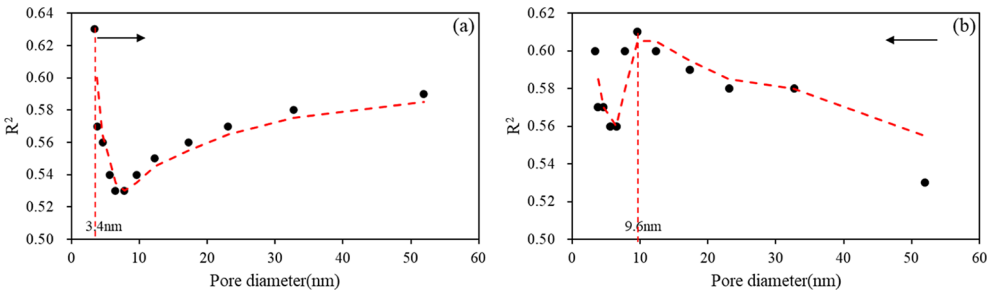

Figure 15. R^2 of linear regression between cumulative dV/dD and the V_{abs} vs pore diameter. (a) Different pore diameter's R^2 determined by the micropore filling mode and (b) different pore diameter's R^2 determined by the monolayer adsorption mode.

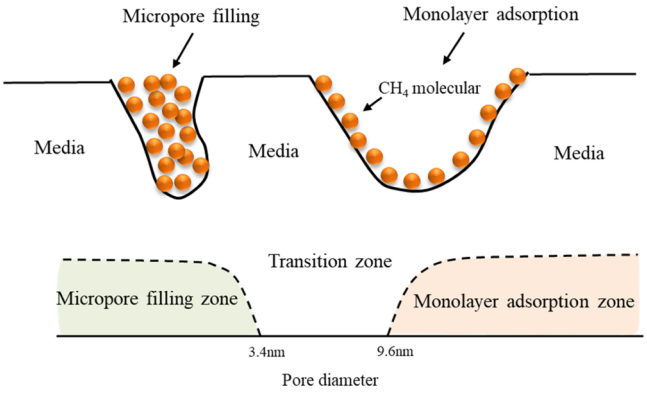

Figure 16. Adsorption mode of methane under different pore sizes. The micropore filling mode is mainly suitable for the methane adsorption in pores smaller than 3.4 nm, and the monolayer adsorption model is more in line with pores larger than 9.6 nm.

study area. Methane adsorption in pores smaller than 3.4 nm is mainly a micropore filling mode, and methane adsorption in pores between 9.6 and 50 nm is mainly a monolayer mode. The intermediate region between 3.4 and 9.6 nm is the transition zone where the monolayer adsorption changes to micropore filling as the pore diameter decreases. In this work, the methane adsorption mechanisms of different lithofacies with different pore structures are clarified from the Upper Triassic lacustrine shales in the western Sichuan Basin, China.

AUTHOR INFORMATION

Corresponding Author

Dongxia Chen − *State Key Laboratory of Petroleum Resources and Prospecting and College of Geosciences, China University of Petroleum, Beijing 102200, China*; Email: lindachen@cup.edu.cn

Authors

Ziyi Liu − *State Key Laboratory of Petroleum Resources and Prospecting and College of Geosciences, China University of Petroleum, Beijing 102200, China*; orcid.org/0000-0002-2071-7469

Siyuan Chang − *State Key Laboratory of Petroleum Resources and Prospecting and College of Geosciences, China University of Petroleum, Beijing 102200, China*

Xiaoliang Wei − *Key Laboratory of Shale Gas Exploration and Evaluation (Ministry of Land and Resources), China University of Geosciences (Beijing), Beijing 100083, China*

Xiuxiang Lv − *State Key Laboratory of Petroleum Resources and Prospecting and College of Geosciences, China University of Petroleum, Beijing 102200, China*

Rusi Zuo − *State Key Laboratory of Marine Geology, Tongji University, Shanghai 200092, China*

Meiling Han − *Key Laboratory of Shale Gas Exploration and Evaluation (Ministry of Land and Resources), China University of Geosciences (Beijing), Beijing 100083, China*

Complete contact information is available at: https://pubs.acs.org/10.1021/acs.energyfuels.1c01345

Author Contributions

Conceptualization, Z.L. and D.C.; methodology, Z.L.; software, S.C.; validation, X.W., X.L., and R.Z.; formal analysis, M.H.; investigation, Z.L.; resources, D.C.; writing—original draft preparation, Z.L.; writing—review and editing, Z.L.; visualization, Z.L.; supervision, Z.L.; project administration, D.C.; and funding acquisition, D.C.

Notes

The authors declare no competing financial interest.

ACKNOWLEDGMENTS

This work was supported by The National Major Science and Technology Projects of China (2016ZX05034-001-005).

REFERENCES

(1) Caineng, Z.; Shizhen, T.; Rukai, Z.; Xuanjun, Y.; Wei, L.; Guangya, Z.; Xiangxiang, Z.; Xiaohui, G.; Liuhong, L.; Chunchun, X. Formation and distribution of "continuous" gas reservoirs and their giant gas province: a case from the Upper Triassic Xujiahe Formation giant gas province, Sichuan Basin. *Pet. Explor. Dev.* **2009**, *36*, 307−319.

(2) Wenzhi, Z.; Hongjun, W.; Chunchun, X.; Congsheng, B.; Zecheng, W.; Xiaohui, G. Reservoir forming mechanism and enrichment conditions of the extensive Xujiahe Formation gas reservoirs, Central Sichuan Basin. *Pet. Explor. Dev.* **2010**, *37*, 146−157.

(3) Li, Y.; Shao, L.; Eriksson, K. A.; Tong, X.; Gao, C.; Chen, Z. Linked sequence stratigraphy and tectonics in the Sichuan continental foreland basin, Upper Triassic Xujiahe Formation, Southwest China. *J. Asian Earth Sci.* **2014**, *88*, 116−136.

(4) Xu, C.; Gehenn, J.-M.; Zhao, D.; Xie, G.; Teng, M.-K. The fluvial and lacustrine sedimentary systems and stratigraphic correlation in the Upper Triassic Xujiahe Formation in Sichuan Basin, China. *Am. Assoc. Pet. Geol. Bull.* **2015**, *99*, 2023−2041.

(5) Tuo, J.; Wu, C.; Zhang, M. Organic matter properties and shale gas potential of Paleozoic shales in Sichuan Basin, China. *J. Nat. Gas Sci. Eng.* **2016**, *28*, 434−446.

(6) Ambrose, R. J.; Hartman, R. C.; Diaz-Campos, M.; Akkutlu, I. Y.; Sondergeld, C. H. Shale gas-in-place calculations part: New pore-scale considerations. *SPE J.* **2012**, *17*, 219−229.

(7) Li, J.; Wu, Q.; Jin, W.; Lu, J.; Nan, Z. Logging evaluation of free-gas saturation and volume content in Wufeng-Longmaxi organic-rich shales in the Upper Yangtze Platform, China. *Mar. Pet. Geol.* **2019**, *100*, 530−539.

(8) Curtis, J. B. Fractured shale − gas systems. *AAPG Bull.* **2002**, *86*, 1921−1938.
(9) Javadpour, F.; Fisher, D.; Unsworth, M. Nanoscale gas flow in shale gas sediments. *J. Can. Pet. Technol.* **2007**, *46*, PETSOC-07-10-06.
(10) Shtepani, E.; Noll, L. A.; Elrod, L. W.; Jacobs, P. M. A new regression-based method for accurate measurement of coal and shale gas content. *SPE Reservoir Eval. Eng.* **2010**, *13*, 359−364.
(11) Etminan, S.; Javadpour, F.; Maini, B. B.; Chen, Z. X. Measurement of gas storage processes in shale and of the molecular diffusion coefficient in kerogen. *Int. J. Coal Geol.* **2014**, *123*, 10−19.
(12) Tian, H.; Li, T.; Zhang, T.; Xiao, X. Characterization of methane adsorption on overmature Lower Silurian-Upper Ordovician shales in Sichuan Basin, southwest China: Experimental results and geological implications. *Int. J. Coal Geol.* **2016**, *156*, 36−49.
(13) Zhou, S.; Wang, H.; Xue, H.; Guo, W.; Li, X. Supercritical methane adsorption on shale gas: Mechanism and model. *Chin. Sci. Bull.* **2017**, *62*, 4189−4200.
(14) Dang, W.; Zhang, J.; Nie, H.; Wang, F.; Tang, X.; Wu, N.; Chen, Q.; Wei, X.; Wang, R. Isotherms, thermodynamics and kinetics of methane-shale adsorption pair under supercritical condition: Implications for understanding the nature of shale gas adsorption process. *Chem. Eng. J.* **2020**, *383*, 123191.
(15) Sudibandriyo, M.; Pan, Z.; Fitzgerald, J. E.; Robinson, R. L.; Gasem, K. A. M. Adsorption of methane, nitrogen, carbon dioxide, and their binary mixtures on dry activated carbon at 318.2 K and pressures up to 13.6 MPa. *Langmuir* **2003**, *19*, 5323−5331.
(16) Richard, M.-A.; Bénard, P.; Chahine, R. Gas adsorption process in activated carbon over a wide temperature range above the critical point. Part 1: Modified Dubinin-Astakhov model. *Adsorption* **2009**, *15*, 43−51.
(17) Ren, W.; Li, G.; Tian, S.; Sheng, M.; Geng, L. Adsorption and Surface Diffusion of Supercritical Methane in Shale. *Ind. Eng. Chem. Res.* **2017**, *56*, 3446−3455.
(18) Gasparik, M.; Ghanizadeh, A.; Bertier, P.; Gensterblum, Y.; Bouw, S.; Krooss, B. M. High-pressure methane sorption isotherms of black shales from the Netherlands. *Energy Fuels* **2012**, *26*, 4995−5004.
(19) Rexer, T. F. T.; Benham, M. J.; Aplin, A. C.; Thomas, K. M. Methane adsorption on shale under simulated geological temperature and pressure conditions. *Energy Fuels* **2013**, *27*, 3099−3109.
(20) Wang, Z.; Li, Y.; Guo, P.; Meng, W. Analyzing the Adaption of Different Adsorption Models for Describing the Shale Gas Adsorption Law. *Chem. Eng. Technol.* **2016**, *39*, 1921−1932.
(21) Tang, X.; Ripepi, N.; Rigby, S.; Mokaya, R.; Gilliland, E. New perspectives on supercritical methane adsorption in shales and associated thermodynamics. *J. Ind. Eng. Chem.* **2019**, *78*, 186−197.
(22) Zhang, J.; Clennell, M. B.; Liu, K.; Pervukhina, M.; Chen, G.; Dewhurst, D. N. Methane and carbon dioxide adsorption on illite. *Energy Fuels* **2016**, *30*, 10643−10652.
(23) Chen, G. H.; Lu, S. F.; Liu, K. Y.; Xu, C. X.; Xue, Q. Z.; Tian, S. S.; Li, J. B.; Lu, S. D.; Zhang, Y. Y. Occurrence State and Micro Mechanisms of Shale Gas on Pore Walls. *Earth Sci.* **2020**, *45*, 1782−1790.
(24) Zhang, T.; Ellis, G. S.; Ruppel, S. C.; Milliken, K.; Yang, R. Effect of organic matter type and thermal maturity on methane adsorption in shale gas systems. *Org. Geochem.* **2012**, *47*, 120−131.
(25) Chareonsuppanimit, P.; Mohammad, S. A.; Robinson, R. L.; Gasem, K. A. M. High-pressure adsorption of gases on shales: Measurements and modeling. *Int. J. Coal Geol.* **2012**, *95*, 34−46.
(26) Zhu, H.; Ju, Y.; Huang, C.; Chen, F.; Chen, B.; Yu, K. Microcosmic gas adsorption mechanism on clay-organic nanocomposites in a marine shale. *Energy* **2020**, *197*, 117256.
(27) Saffron, C. M.; Park, J.-H.; Dale, B. E.; Voice, T. C. Kinetics of contaminant desorption from soil: comparison of model formulations using the Akaike information criterion. *Environ. Sci. Technol.* **2006**, *40*, 7662−7667.
(28) Spiess, A.-N.; Neumeyer, N. An evaluation of R^2 as an inadequate measure for nonlinear models in pharmacological and biochemical research: a Monte Carlo approach. *BMC Pharmacol.* **2010**, *10*, 6.
(29) Yao, Y.; Liu, D.; Tang, D.; Tang, S.; Huang, W. Fractal characterization of adsorption-pores of coals from North China: an investigation on CH4 adsorption capacity of coals. *Int. J. Coal Geol.* **2008**, *73*, 27−42.
(30) Xu, H.; Zhou, W.; Zhang, R.; Liu, S.; Zhou, Q. Characterizations of pore, mineral and petrographic properties of marine shale using multiple techniques and their implications on gas storage capability for Sichuan Longmaxi gas shale field in China. *Fuel* **2019**, *241*, 360−371.
(31) Wang, S.; Dong, D.; Wang, Y.; Li, X.; Huang, J.; Guan, Q. Sedimentary geochemical proxies for palaeoenvironment interpretation of organic-rich shale: a case study of the Lower Silurian Longmaxi Formation, Southern Sichuan Basin, China. *J. Nat. Gas Sci. Eng.* **2016**, *28*, 691−699.
(32) Li, Z.; Schieber, J. Detailed facies analyses of the Upper Cretaceous Tununk Shale Member, Henry Mountains Region, Utah: Implications for mudstone depositional models in epicontinental seas. *Sediment. Geol.* **2018**, *364*, 141−159.
(33) Huang, J.; Zou, C.; Dong, D.; Li, J.; Wang, Y.; Wang, S.; Li, D. Geochemical and reservoir characteristics of the Upper Triassic continental shale in the Sichuan Basin, China. *Energy Explor. Exploit.* **2015**, *33*, 375−395.
(34) Wang, P.; Shen, Z.-M.; Liu, S.-B.; Lü, Z.-X.; Feng, J.-R.; Wang, J.-Z. The geochemical characteristics and comparison of the terrestrial natural gas in sichuan basin. *Nat. Gas Geosci.* **2013**, *24*, 1186−1195.
(35) Yang, W.; Zuo, R.; Chen, D.; Jiang, Z.; Guo, L.; Liu, Z.; Chen, R.; Zhang, Y.; Zhang, Z.; Song, Y.; Luo, Q.; Wang, Q.; Wang, J.; Chen, L.; Li, Y.; Zhang, C. Climate and tectonic-driven deposition of sandwiched continental shale units: New insights from petrology, geochemistry, and integrated provenance analyses (the western Sichuan subsiding Basin, Southwest China). *Int. J. Coal Geol.* **2019**, *211*, 103227.
(36) Shen, Y.; Ge, H.; Li, C.; Yang, X.; Ren, K.; Yang, Z.; Su, S. Water imbibition of shale and its potential influence on shale gas recovery−a comparative study of marine and continental shale formations. *J. Nat. Gas Sci. Eng.* **2016**, *35*, 1121−1128.
(37) Gao, Z.; Yang, S.; Jiang, Z.; Zhang, K.; Chen, L. Investigating the spontaneous imbibition characteristics of continental Jurassic Ziliujing Formation shale from the northeastern Sichuan Basin and correlations to pore structure and composition. *Mar. Pet. Geol.* **2018**, *98*, 697−705.
(38) Wang, L.; Guo, Y.; Yang, C.; Xiao, J.; Lu, C.; Song, Y. Mechanical characterization of continental shale in Sichuan Basin of China and its potential impact on reservoir stimulation. *J. Nat. Gas Sci. Eng.* **2020**, *79*, 103346.
(39) Liu, Y.; Chen, D.; Qiu, N.; Fu, J.; Jia, J. Geochemistry and origin of continental natural gas in the western Sichuan basin, China. *J. Nat. Gas Sci. Eng.* **2018**, *49*, 123−131.
(40) Rukai, Z.; Xia, Z.; Liuhong, L.; Xuesong, W.; Nai, Z.; Hongil, G.; Lihong, S. Depositional system and favorable reservoir distribution of Xujiahe Formation in Sichuan Basin. *Pet. Explor. Dev.* **2009**, *36*, 46−55.
(41) Chalmers, G. R. L.; Bustin, R. M. Lower Cretaceous gas shales in northeastern British Columbia. Part I: geological controls on methane sorption capacity. *Bull. Can. Pet. Geol.* **2008**, *56*, 1−21.
(42) Barrett, E. P.; Joyner, L. G.; Halenda, P. P. The determination of pore volume and area distribution in porous substances. I. Computations from nitrogen isotherms. *J. Am. Chem. Soc.* **1951**, *73*, 373−380.
(43) Kuila, U.; Prasad, M. Specific surface area and pore-size distribution in clays and shales. *Geophys. Prospect.* **2013**, *61*, 341−362.
(44) Clarkson, C. R.; Solano, N.; Bustin, R. M.; Bustin, A. M. M.; Chalmers, G. R. L.; He, L.; Melnichenko, Y. B.; Radliński, A. P.; Blach, T. P. Pore structure characterization of North Americould shale gas reservoirs using USANS/SANS, gas adsorption, and mercury intrusion. *Fuel* **2013**, *103*, 606−616.
(45) Guo, X.; Qin, Z.; Yang, R.; Dong, T.; He, S.; Hao, F.; Yi, J.; Shu, Z.; Bao, H.; Liu, K. Comparison of pore systems of clay-rich and silica-rich gas shales in the lower Silurian Longmaxi formation from the Jiaoshiba area in the eastern Sichuan Basin, China. *Mar. Pet. Geol.* **2019**, *101*, 265−280.
(46) Brunauer, S.; Emmett, P. H.; Teller, E. Adsorption of gases in multimolecular layers. *J. Am. Chem. Soc.* **1938**, *60*, 309−319.

https://doi.org/10.1021/acs.energyfuels.1c01345
Energy Fuels 2021, 35, 13654−13670

(47) Qi, H.; Ma, J.; Wong, P.-z. Adsorption isotherms of fractal surfaces. *Colloids Surf., A* **2002**, *206*, 401−407.
(48) Pyun, S.-I.; Rhee, C.-K. An investigation of fractal characteristics of mesoporous carbon electrodes with various pore structures. *Electrochim. Acta* **2004**, *49*, 4171−4180.
(49) Rigby, S. P. Predicting surface diffusivities of molecules from equilibrium adsorption isotherms. *Colloids Surf., A* **2005**, *262*, 139−149.
(50) Hu, H.; Zhang, T.; Wiggins-Camacho, J. D.; Ellis, G. S.; Lewan, M. D.; Zhang, X. Experimental investigation of changes in methane adsorption of bitumen-free Woodford Shale with thermal maturation induced by hydrous pyrolysis. *Mar. Pet. Geol.* **2014**, *59*, 114−128.
(51) Krooss, B. M.; van Bergen, F.; Gensterblum, Y.; Siemons, N.; Pagnier, H. J. M.; David, P. High pressure CH_4 and carbon dioxide adsorption on dry and moisture equilibrated Pennsylvanian coals. *Int. J. Coal Geol.* **2002**, *51*, 69−92.
(52) Ji, W.; Song, Y.; Jiang, Z.; Wang, X.; Bai, Y.; Xing, J. Geological controls and estimation algorithms of lacustrine shale gas adsorption capacity: a case study of the Triassic strata in the southeastern ordos basin, China. *Int. J. Coal Geol.* **2014**, *134−135*, 61−73.
(53) Langmuir, I. The adsorption of gases on plane surfaces of glass, mica and platinum. *J. Am. Chem. Soc.* **1918**, *40*, 1361−1403.
(54) Larsen, J. W. The effects of dissolved CO_2 on coal structure and properties. *Int. J. Coal Geol.* **2004**, *57*, 63−70.
(55) Sakurovs, R.; Day, S.; Weir, S.; Duffy, G. Application of a modified Dubinin−Radushkevich equation to adsorption of gases by coals under supercritical conditions. *Energy Fuels* **2007**, *21*, 992−997.
(56) Dubinin, M. M.; Astakhov, V. A. Development of the concepts of volume filling of micropores in the adsorption of gases and vapors by microporous adsorbents. *Bull. Acad. Sci. USSR, Div. Chem. Sci.* **1971**, *20*, 3−7.
(57) Busch, A.; Gensterblum, Y.; Krooss, B. M.; Littke, R. Methane and carbon dioxide adsorption−diffusion experiments on coal: upscaling and modeling. *Int. J. Coal Geol.* **2004**, *60*, 151−168.
(58) Hu, H.; Hao, F.; Guo, X.; Dai, F.; Lu, Y.; Ma, Y. Investigation of methane sorption of overmature Wufeng-Longmaxi shale in the Jiaoshiba area, Eastern Sichuan Basin, China. *Mar. Pet. Geol.* **2018**, *91*, 251−261.
(59) Ruckenstein, E.; Vaidyanathan, A. S.; Youngquist, G. R. Sorption by solids with bidisperse pore structures. *Chem. Eng. Sci.* **1971**, *26*, 1305−1318.
(60) Ross, D. J. K.; Marc Bustin, R. The importance of shale composition and pore structure upon gas storage potential of shale gas reservoirs. *Mar. Pet. Geol.* **2009**, *26*, 916−927.

https://doi.org/10.1021/acs.energyfuels.1c01345
Energy Fuels 2021, 35, 13654−13670